



**HAL**  
open science

# Quasi-Static Homogenization of Glide-Symmetric Holey Parallel-Plate Waveguides with Ultra-Wideband Validity

Boris Fischer, Guido Valerio

► **To cite this version:**

Boris Fischer, Guido Valerio. Quasi-Static Homogenization of Glide-Symmetric Holey Parallel-Plate Waveguides with Ultra-Wideband Validity. *IEEE Transactions on Antennas and Propagation*, 2022, 70 (11), pp.10569 - 10582. 10.1109/TAP.2022.3187527 . hal-03427816v2

**HAL Id: hal-03427816**

**<https://hal.science/hal-03427816v2>**

Submitted on 4 Jan 2024

**HAL** is a multi-disciplinary open access archive for the deposit and dissemination of scientific research documents, whether they are published or not. The documents may come from teaching and research institutions in France or abroad, or from public or private research centers.

L'archive ouverte pluridisciplinaire **HAL**, est destinée au dépôt et à la diffusion de documents scientifiques de niveau recherche, publiés ou non, émanant des établissements d'enseignement et de recherche français ou étrangers, des laboratoires publics ou privés.

# Quasi-Static Homogenization of Glide-Symmetric Holey Parallel-Plate Waveguides with Ultra-Wideband Validity

Boris Fischer, and Guido Valerio, *Senior Member, IEEE*

**Abstract**—Glide-symmetric waveguides made of metallic meta-surfaces are a wideband, low-loss, low-cost, and conformable alternative to dielectric materials for the design of antenna lenses at millimeter waves. However, computing the effective refractive index of glide-symmetric waveguides with existing full-wave analysis techniques results in cumbersome parametric studies for each new design. This paper presents a new analytic homogenization technique for glide-symmetric holey parallel-plate waveguides. The dispersion equation of these structures, found by way of mode-matching, is simplified at low frequency using the properties of the modes resonating within the holes, independently of the hole shape. This simplified equation yields a closed-form expression of the effective refractive index, relying on the eigenmodes of the hole cross-section. This formula avoids solving a three-dimensional full-wave problem, and is fully analytic in the case of canonical hole shapes. Although derived in the quasi-static regime, it characterizes propagation over an ultra-wide band, due to the low dispersive properties of glide symmetric structures. It is a function of the angle of propagation within the waveguide, and can thus be used to study anisotropic properties. Its efficiency is demonstrated with the example of glide-symmetric parallel-plate waveguides with rectangular and circular holes.

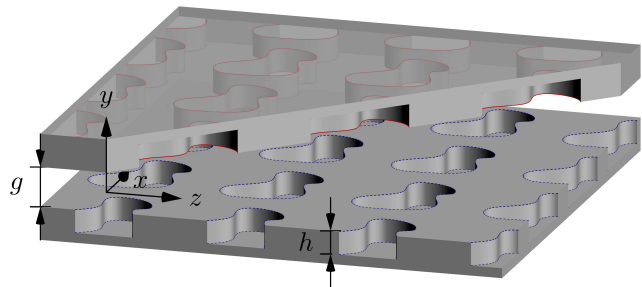
**Index Terms**—Metasurfaces, glide symmetry, mode-matching, periodic problems, analytic methods, homogenization

## I. INTRODUCTION

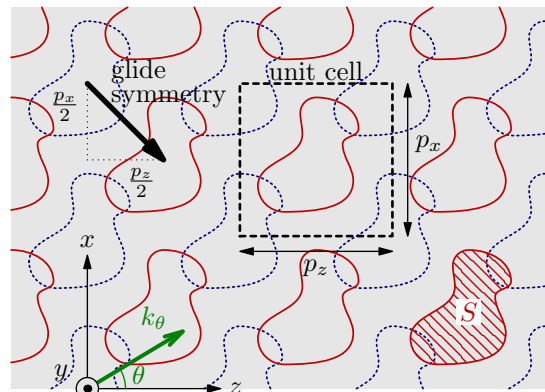
**I**N the advent of the internet of things and 5G/6G mobile networks, modern wireless communication systems must meet the needs of increasingly many connected users and devices [1]–[4]. High data rates in relation to limited space-time-frequency resources involve the need for millimeter wave antennas with dynamically orientable beam [5], [6]. Existing beam-forming arrays are bulky and tend to be expensive at millimeter waves [7], [8], which motivates the use of near-optical solutions such as lens antennas [9]. Such lenses have been built by adding different dielectric layers in an onion-like manner to gradually change the refractive index [10]–[12]. Compact and conformable designs can be obtained with planar lenses, which can be further compressed by applying transformation

Boris Fischer and Guido Valerio are with Sorbonne Université, CNRS, Laboratoire Génie électrique et électronique de Paris, 75252, Paris, France and with Université Paris-Saclay, CentraleSupélec, CNRS, Laboratoire de Génie Électrique et Electronique de Paris, 91192, Gif-sur-Yvette, France (e-mail: boris.fischer@sorbonne-universite.fr, guido.valerio@sorbonne-universite.fr).

This work has been submitted to the IEEE for possible publication. Copyright may be transferred without notice, after which this version may no longer be accessible. This work was supported by the French government under the ANR grant HOLeYMETA ANR JCJC 2016 ANR-16-CE24-0030. This publication is based upon work from COST Action Symat (CA18223), supported by COST (European Cooperation in Science and Technology).



(a) Perspective view



(b) Top view

Fig. 1. Holey glide-symmetric parallel-plate waveguide. To highlight the glide-symmetric shift between the two plates, the upper holes are outlined with red, in opposition to dashed blue for the lower holes. In the top view (b), one unit cell of this metasurface waveguide is framed, and the propagation direction of angle  $\theta$  is indicated with the wavenumber  $k_\theta$ .

optics [13], [14]. However, these lenses are lossy, expensive, and have limited performances due to the use of dielectric materials. An alternative is to build integrated lenses using planar waveguides made of metasurfaces [15]. Due to the sub-wavelength geometry of the periodically repeated unit cells, a smooth profile of the effective refractive index can be accurately controlled by varying their characteristic dimensions [16]–[20]. To avoid dielectric losses, all-metallic designs are preferable, where a parallel-plate waveguide (PPW) is formed of two metasurfaces facing each other, shielding and confining the waves propagating between them [21].

In recent years, it has been shown that the dispersive behavior and the refractive index range of such PPW can be improved using glide symmetry (GS) [22]. GS is a special type of higher symmetry, where the geometry of the waveguide is

invariant after a translation of half-a-unit-cell and a reflection with respect to a plane. As such, compared to previous non-glide designs, it is enough to shift the upper metasurface by half-a-period with respect to the lower metasurface to obtain GS, as illustrated in Fig. 1. Glide-symmetric (GS) waveguides have first been studied in the late 1960s and early 1970s in the context of high-power slow-wave structures [23]–[25]. Not only has this added symmetry been shown to enhance the refractive index of the all-metallic waveguide, but also the dispersive behavior of the structure is mitigated, due to the disappearance of the bandgap between the first and second propagating modes [26]. GS also offers a higher anisotropic behavior than non-glide designs, leading to wideband lenses compressed with transformation optics [27]. Wideband low-loss lenses have been designed using various metasurface unit cells [22], [27]–[30]. Nevertheless, these designs rely on cumbersome parametric studies: for each set of dimensions, the effective refractive index of the unit cell is computed numerically, either with commercial solvers, or with the aforementioned semi-analytical methods [31]–[33].

The interesting features of GS PPWs reach their full potential when the gap between the two metasurfaces is very small compared to the other characteristic dimensions of the unit cell. This contrast in size leads to the wideband properties of the waveguide, but also makes numerical commercial solvers prohibitively slow to analyze them. Existing analytic methods for metasurfaces, like the homogenization of the two independent metasurfaces [34], [35] fail to capture the coupling of higher modes between the variations of the upper and lower metasurfaces [36], which cannot be neglected due to the small gap. Equivalent circuit methods are limited to geometries where the upper and lower geometrical variations do not overlap [37], [38]. Recently, a semi-analytic method based on the multimodal transfer matrix of one cell was able to accurately derive the dispersion equation of GS waveguides [39]. By combining it with a generalization of the Floquet theorem for GS [25], this method reduces the problem to one half (1D GS) or one quarter (2D GS) of the total unit cell. The resulting fast analysis method has since been used in various applications [33], [40]–[42]. While this multimodal transfer matrix method can be applied to any non-canonical cell geometry, it relies on commercial solvers to compute the transfer matrix. An alternative method applicable to holey GS PPWs is presented in [43] for square holes, based on a mode-matching method (MMM). It is generalized in [44] for any hole cross-section, and has since been applied to triangular [45] and elliptical [46] holes in the context of anisotropic waveguides. This method is based on ensuring the continuity of the fields between different regions of the waveguide. Both the multimodal transfer matrix method and the MMM are much faster than full-wave solvers, and have the advantage of computing not only the real but also the imaginary part of the effective wavenumber. Nevertheless, these multimodal methods yield a complicated dispersion equation that must be solved numerically to obtain this wavenumber. If a large number of modes are needed to describe the fields, which is often the case due to the strong interaction between the close metasurfaces, finding this complex solution can still require

extensive computational resources.

In this paper, the core idea is to rely on the dispersive properties of GS waveguides to find a closed-form solution of the effective refractive index of a holey GS PPW. In Section II, the structure under study is presented, and its dispersion equation is derived by means of the MMM presented in [44]. In Section III, this dispersion equation is simplified at low frequencies, and is shown to have a closed-form solution for the effective refractive index, given in (34). Due to the low-dispersive behavior of the waveguide, this low-frequency index is valid over a large frequency band. In Section IV, this method is applied to holey GS PPWs with rectangular and circular holes.

## II. MODE-MATCHING TECHNIQUE USING THE GENERALIZED FLOQUET THEOREM

In this section, the structure under study is presented and its fields are described as sums of modes and harmonics. Boundary conditions are enforced by a MMM based on the generalized Floquet theorem, which leads to a dispersion equation describing the propagation within the waveguide [44].

### A. Glide-symmetric holey parallel-plate waveguide

A holey GS PPW is considered in Fig. 1. It is made of two metallic metasurfaces facing each other in the  $zx$  plane, separated by an empty gap  $g$  (permittivity  $\epsilon_0$  and permeability  $\mu_0$ ). The metasurfaces are assumed to be made of a perfect electric conductor (PEC) material (infinite permittivity). Cylindrical holes with arbitrary cross-section of surface  $S$  are repeated periodically in both upper and lower plates, forming a rectangular lattice of periods  $p_z$  and  $p_x$ , along the  $z$  and  $x$  axis, respectively. These holes have a depth  $h$  and do not go through the PEC plates. They may be filled with a dielectric medium of relative permittivity  $\epsilon_r$  and permeability  $\mu_r$ . Finally, two-dimensional GS is introduced in the structure by shifting the upper holes by  $p_z/2$  in the  $z$  direction, and by  $p_x/2$  in the  $x$  direction. As such, one unit-cell of this waveguide comprises a rectangle of size  $p_z \times p_x$  in the  $zx$ -plane, as indicated by the dashed frame in Fig. 1.

A time-harmonic wave with frequency  $f = 2\pi\omega$  is propagating in the  $zx$ -plane between the two metasurfaces. The corresponding free-space wavenumber in vacuum is defined as  $k = \omega/c_0$ , where  $c_0$  is the free-space velocity of light. The wavelength  $\lambda = c_0/f$  is large compared to the above-mentioned dimensions of each unit cell. For a structure with cells of a few millimeters, this implies operating frequencies up to several tens of gigahertz.

The propagation of the wave between the two metasurfaces is characterized by the angle  $\theta$  between the propagation direction and the  $z$ -axis, as shown in Fig. 1. At the operating frequency, the effective wavenumber of the wave is called  $k_\theta$ , with cartesian components  $k_z$  and  $k_x$ . In order for the wave to be confined within the waveguide and to propagate in the  $\theta$ -direction, the effective wavenumber must satisfy  $k_\theta \geq k$ . The effective refractive index of the waveguide in the  $\theta$ -direction

is defined as  $n_\theta = k_\theta/k$ . This refractive index is related to the cartesian components with

$$k_z = kn_\theta \cos \theta \quad \text{and} \quad k_x = kn_\theta \sin \theta. \quad (1)$$

At a given frequency, the goal is to compute the corresponding effective refractive index  $n_\theta$ . In order to do so, the dispersion equation of the structure needs to be derived.

### B. Mode-matching method

The MMM for a holey GS PPW has been introduced in [44]. Here, it is briefly presented with the formalism suitable for the homogenization discussed in Section III. The electric and magnetic fields in the structure are decomposed as sums of modes and harmonics, whose coefficients are unknown. The MMM then enforces boundaries between different regions in order to obtain a set of equations, that can be solved for the coefficients of the fields. The structure is separated into three regions: the holes in the lower metasurface, the gap between the metasurfaces, and the holes in the upper metasurface. Due to the periodicity of the waveguide, the fields in neighboring cells can be related using the Floquet theorem [47, p. 607]. This theorem is generalized in [25] in order to relate the fields between the upper and lower hole in a GS structure. As such, it is enough to study the fields in half-a-unit-cell of the waveguide.

On the one hand, in the gap, the periodicity of the structure in both  $z$  and  $x$  directions enables the decomposition of the fields as a sum of Floquet harmonics. Each harmonic is defined by a pair of integer indices  $(s, \ell)$  with corresponding wavenumbers

$$k_z^{(s)} = k_z + s \frac{2\pi}{p_z} \quad \text{and} \quad k_x^{(\ell)} = k_x + \ell \frac{2\pi}{p_x}, \quad (2)$$

which characterize the propagation of the harmonic in  $z$  and  $x$  directions with respect to the fundamental harmonic wavenumbers defined in (1).

On the other hand, the holes can be seen as cylindrical waveguides with propagation in the  $y$  direction, where the fields are decomposable as a sum of transverse magnetic (TM) and transverse electric (TE) modes, designated by mode orders  $m \in \mathbb{N}$ . Because a PEC boundary closes the holes, the modes are reflected at the bottom, resulting in standing waves. At the surface of the hole, the tangential electric field of each mode is  $e_{t,m}^i(z, x)$  for the  $m$ th mode, where  $t$  stands for transverse, and with  $i = e, h$  for TM and TE modes, respectively. These modal functions are frequency-independent and real. The corresponding cut-off frequency is  $k_m^i$ . The wave admittances for TM and TE modes are [48, pp. 100-101]

$$Y_m^e = \frac{k\epsilon_r}{\eta \sqrt{k^2 \epsilon_r \mu_r - k_m^e{}^2}} \quad \text{and} \quad Y_m^h = \frac{\sqrt{k^2 \epsilon_r \mu_r - k_m^h{}^2}}{\eta k \mu_r}, \quad (3)$$

where  $\eta = \sqrt{\mu_0/\epsilon_0}$  is the vacuum wave impedance. The squared norm of each transverse waveguide mode is defined as

$$I_m^i = \iint_S e_{t,m}^i \cdot e_{t,m}^i ds. \quad (4)$$

In order to enforce the continuity of the tangential electric and magnetic fields along the surface of the hole, the MMM projects the waveguide modes onto the Floquet harmonics. For each TM and TE mode of order  $m$ , one calls its projection onto the Floquet harmonic  $(s, \ell)$  the projected modal function (PMF), defined as

$$\tilde{e}_{t,m}^{i(s\ell)} = \iint_S e_{t,m}^i(z, x) F^{(s\ell)} ds, \quad (5)$$

with  $F^{(s\ell)} = e^{-jk_z^{(s)}z - jk_x^{(\ell)}x}$  the propagation term of the Floquet harmonic. The PMF can be interpreted as the Fourier transform of the modal function with Fourier variables  $(k_z^{(s)}, k_x^{(\ell)})$ .

Combining the field continuity equations leads to a system of equations involving the PMFs. In practice, a finite number  $M^e$  of TM modes and  $M^h$  of TE modes can be considered so that the system matrix has finite dimensions. In order for this system to have a non-trivial solution i.e., for the fields in the structure to be non-zero, the determinant of this matrix must be null. This yields the dispersion equation of the holey GS PPW

$$\begin{vmatrix} M^{e,e} & (M^{h,e})^H \\ M^{h,e} & M^{h,h} \end{vmatrix} = 0, \quad (6)$$

where  $\cdot^H$  designates the hermitian of a matrix. Each row and each column of the total square matrix in (6) corresponds to a specific TM or TE mode. The equations have been arranged such that this matrix can be divided in four parts.  $M^{e,e}$  and  $M^{h,h}$  are square matrices that involve only TM and TE modes, respectively, and as such they have sizes  $M^e \times M^e$  and  $M^h \times M^h$ , respectively.  $M^{h,e}$  has TE rows and TM columns, and is square only if  $M^h = M^e$ . The coefficients of these matrices are

$$\begin{aligned} (M^{i',i})_{m',m} &= \delta_{i'i'} \delta_{mm'} k \eta p_x p_z I_m^i Y_m^i \cot \left( h \sqrt{k^2 \epsilon_r \mu_r - k_m^i{}^2} \right) \\ &+ \sum_{\ell, s} f^{(s\ell)} \begin{bmatrix} k^2 \left( \tilde{e}_{x,m'}^{i'(s\ell)} \tilde{e}_{x,m}^{i(s\ell)*} + \tilde{e}_{z,m'}^{i'(s\ell)} \tilde{e}_{z,m}^{i(s\ell)*} \right) \\ - \left( k_z^{(s)} \tilde{e}_{x,m'}^{i'(s\ell)} - k_x^{(\ell)} \tilde{e}_{z,m'}^{i'(s\ell)} \right) \\ \cdot \left( k_z^{(s)} \tilde{e}_{x,m}^{i(s\ell)} - k_x^{(\ell)} \tilde{e}_{z,m}^{i(s\ell)} \right)^* \end{bmatrix}, \quad (7) \end{aligned}$$

where the Kronecker symbol  $\delta_{mm'}$  takes the value 1 when  $m' = m$ , and 0 otherwise. The row and column indices  $m'$  and  $m$  correspond to TM and/or TE modes, depending on the considered quarter of the dispersion matrix. The cartesian components of the PMFs are written  $\tilde{e}_{z,m}^{i(s\ell)}$  and  $\tilde{e}_{x,m}^{i(s\ell)}$ . For conciseness,  $\sum$  represents the double sum over all pairs of harmonic indices  $(s, \ell) \in \mathbb{Z}^2$ . Although in theory, an infinite number of harmonics  $(s, \ell)$  is involved, in practice it can be truncated to a finite number  $N$  of dominant harmonics. The terms in the sum associated to harmonics  $(s, \ell)$  are referred to as *harmonic terms*. These harmonic terms are dependent

on the vertical spectral function of each Floquet harmonic, defined as

$$f^{(s\ell)} = \begin{cases} \frac{\cot\left(\frac{g}{2}\sqrt{k_z^2 - k_z^{(s)2} - k_x^{(\ell)2}}\right)}{\sqrt{k_z^2 - k_z^{(s)2} - k_x^{(\ell)2}}} & \text{if } s + \ell \text{ is even,} \\ \frac{\tan\left(\frac{g}{2}\sqrt{k_z^2 - k_z^{(s)2} - k_x^{(\ell)2}}\right)}{\sqrt{k_z^2 - k_z^{(s)2} - k_x^{(\ell)2}}} & \text{if } s + \ell \text{ is odd.} \end{cases} \quad (8)$$

This vertical spectral function is a consequence of the field distribution along the  $y$ -axis between the two metasurfaces.

At a given frequency and propagation direction, the only unknowns in (6) are  $k_z$  and  $k_x$ , which are both linked to  $n_\theta$  in (1). As such, solving (6) for  $n_\theta$  makes it possible to draw the Brillouin diagram of the waveguide, thus disclosing the dispersive properties of the waveguide. In the following sections, the goal is to find a closed-form solution of (6).

### III. LOW-FREQUENCY EFFECTIVE REFRACTIVE INDEX

In this section, the dispersion equation (6) is simplified and reformulated at low-frequency i.e., for  $k \rightarrow 0$ , which implies that  $k_z \rightarrow 0$  and  $k_x \rightarrow 0$  according to (1). The goal is to find a closed-form solution of the effective refractive index in this particular case, which remains valid at higher frequencies due to the low dispersion of GS waveguides. As such, the challenge is twofold. First, the dispersion matrix must be carefully reduced at low-frequency such that the frequency-dependency disappears but all relevant  $n_\theta$ -dependencies remain. Second, a closed-form solution must be found for the resulting low-frequency dispersion equation.

#### A. Distinction between fundamental- and higher-harmonic terms at low frequency

At low-frequency, according to (1) and (2), harmonic wavenumbers become

$$\begin{bmatrix} k_z^{(s)} \\ k_x^{(\ell)} \end{bmatrix} \Big|_{\substack{k_z \rightarrow 0 \\ k_x \rightarrow 0}} = \begin{cases} \begin{bmatrix} k_z \\ k_x \end{bmatrix} = \begin{bmatrix} kn_\theta \cos \theta \\ kn_\theta \sin \theta \end{bmatrix} & \text{for } s = \ell = 0, \\ \begin{bmatrix} \frac{s2\pi}{p_z} \\ \frac{\ell 2\pi}{p_x} \end{bmatrix} = \Gamma^{(s\ell)} & \text{for } (s, \ell) \neq (0, 0). \end{cases} \quad (9)$$

as illustrated in Fig. 2. Cases where either  $s$  or  $\ell$  is zero are a particular case, but they can be shown to behave as the other higher harmonics. Therefore, in the following, it is important to distinguish between the fundamental-harmonic terms with  $s = \ell = 0$ , and higher-harmonic terms where  $s \neq 0$  and  $\ell \neq 0$ .

This difference between fundamental and higher harmonics at low frequency is notable for the vertical spectral function defined in (8). On the one hand, for  $\ell = s = 0$ , the vertical spectral function tends to

$$f^{(00)} \Big|_{\substack{k_z \rightarrow 0 \\ k_x \rightarrow 0}} = \bar{f}^{(00)} = \frac{2}{gk^2(1 - n_\theta^2)}, \quad (10)$$

where  $k_z$  and  $k_x$  are replaced by  $n_\theta$  according to (1).

On the other hand, when  $\ell \neq 0$  or  $s \neq 0$ , the vertical spectral function tends to

$$\bar{f}^{(s\ell)} = \begin{cases} -\tanh\left(\frac{g}{2}\Gamma^{(s\ell)}\right)/\Gamma^{(s\ell)} & \text{if } \ell + s \text{ odd,} \\ -\coth\left(\frac{g}{2}\Gamma^{(s\ell)}\right)/\Gamma^{(s\ell)} & \text{if } \ell + s \text{ even,} \end{cases} \quad (11)$$

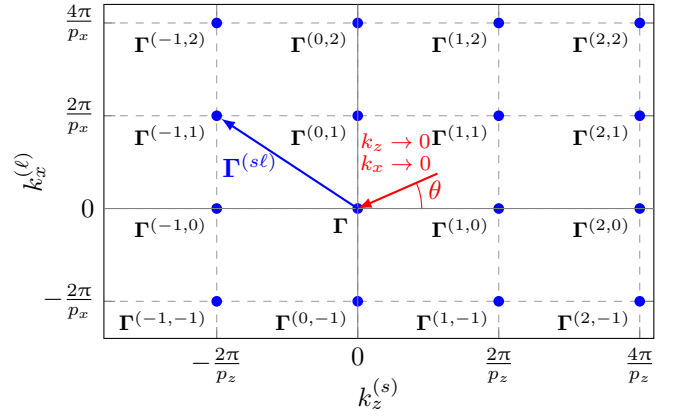


Fig. 2. Spectral domain of the Floquet harmonics. During the homogenization process, the harmonics of orders  $(s, \ell)$  are evaluated at the blue points, which are the periodic replicas of the  $\Gamma$ -point  $(k_z, k_x) = (0, 0)$ . The latter is approached from the propagation direction  $\theta$ , as indicated by the red arrow.

where  $\Gamma^{(s\ell)} = \|\Gamma^{(s\ell)}\|$  is the norm of the low-frequency harmonic wavenumber defined in (9).

#### B. Low-frequency PMFs

The dispersion coefficients (7) are dependent on the PMFs  $\tilde{e}_{t,m}^{i(s\ell)}$  of the hole, defined in (5) as the Fourier transforms of the transverse modal functions  $e_{t,m}^i$ . Consequently, the PMFs are functions of  $k_z^{(s)}$  and  $k_x^{(\ell)}$ , which are here simplified at low frequency according to (9).

For TE modes, the low-frequency simplification of  $\tilde{e}_{t,m}^{h(s\ell)}$  is

$$\begin{bmatrix} \tilde{e}_{z,m}^{h(s\ell)} \\ \tilde{e}_{x,m}^{h(s\ell)} \end{bmatrix} \Big|_{\substack{k_z \rightarrow 0 \\ k_x \rightarrow 0}} = \begin{bmatrix} \tilde{e}_{z,m}^{(s\ell)} \\ \tilde{e}_{x,m}^{(s\ell)} \end{bmatrix} = \iint_S e_{t,m}^i e^{-j\frac{s2\pi}{p_z}z - j\frac{\ell 2\pi}{p_x}x} ds, \quad (12)$$

which is the Fourier transform of the transverse modal function computed at the point  $\Gamma^{(s\ell)}$ .

For TM modes, Appendix A relates the transverse fields to the longitudinal electric modal function  $e_{y,m}$ . The latter's Fourier transform at low frequency is computed at the point  $\Gamma^{(s\ell)}$  as

$$\tilde{e}_{y,m}^{(s\ell)} = \iint_S e_{y,m} e^{-j\frac{s2\pi}{p_z}z - j\frac{\ell 2\pi}{p_x}x} ds. \quad (13)$$

Inserting (13) in (40) yields the low-frequency simplification of  $\tilde{e}_{t,m}^{e(s\ell)}$

$$\begin{bmatrix} \tilde{e}_{z,m}^{e(s\ell)} \\ \tilde{e}_{x,m}^{e(s\ell)} \end{bmatrix} \Big|_{\substack{k_z \rightarrow 0 \\ k_x \rightarrow 0}} = \frac{j}{k_m^e} \Gamma^{(s\ell)} \tilde{e}_{y,m}^{(s\ell)}, \quad (14)$$

for  $(s, \ell) \neq (0, 0)$ , and

$$\begin{bmatrix} \tilde{e}_{z,m}^{e(00)} \\ \tilde{e}_{x,m}^{e(00)} \end{bmatrix} \Big|_{\substack{k_z \rightarrow 0 \\ k_x \rightarrow 0}} = \frac{jk_n\theta}{k_m^e} \begin{bmatrix} \cos \theta \\ \sin \theta \end{bmatrix} \tilde{e}_{y,m}^{(00)}. \quad (15)$$

All low-frequency coefficients  $\tilde{e}_{z,m}^{(s\ell)}$ ,  $\tilde{e}_{x,m}^{(s\ell)}$  and  $\tilde{e}_{y,m}^{(s\ell)}$  are independent of  $k_z$  and  $k_x$ .

### C. Low-frequency simplification of the matrix coefficients

In the following paragraphs, the coefficients of the dispersion matrix are simplified at low frequency, depending on whether TM or TE modes are involved. In (7), these coefficients can be separated in three parts: the diagonal waveguide term, which is only present in the diagonal coefficients of  $M^{e,e}$  and  $M^{h,h}$ , the fundamental-harmonic term, where  $s = \ell = 0$ , and higher-harmonic terms. These terms are simplified separately in the following paragraphs.

1) *Diagonal waveguide term:* The first term out of the summation in (7) is proportional to the Kronecker symbols  $\delta_{ii'}\delta_{mm'}$ , which means that it is non-zero only in the diagonal of  $M^{e,e}$ , and in the diagonal of  $M^{h,h}$ . Due to the absence of transverse electromagnetic (TEM) modes in the holes,  $k^2\epsilon_r\mu_r - k_m^i{}^2 \rightarrow -k_m^i{}^2 \neq 0$  at low frequency, which reduces the admittance expressions (3) and the cotangent terms. Therefore, the low frequency diagonal terms of  $M^{e,e}$  are

$$-k^2\epsilon_r p_x p_z I_m^e \frac{\coth(hk_m^e)}{k_m^e}, \quad (16)$$

appearing to be proportional to  $k^2$ . On the other hand, the diagonal terms of  $M^{h,h}$  become the frequency-independent constants

$$\frac{p_x p_z}{\mu_r} I_m^h k_m^h \coth(hk_m^h). \quad (17)$$

2) *Fundamental-harmonic term:* As explained in paragraph III-A, the fundamental-harmonic term in (7) with  $s = \ell = 0$  must be isolated from higher-harmonic terms. At low frequency, occurrences of  $k_z$  and  $k_x$  as well as the vertical spectral function can be expressed as functions of  $n_\theta$  according to (1) and (10). The  $n_\theta$ -dependencies can then be isolated after reformulating the fundamental-harmonic term as

$$\begin{aligned} & \frac{2}{g(1-n_\theta^2)} \left[ \begin{aligned} & \left( \sin\theta \tilde{e}_{x,m'}^{i(00)} + \cos\theta \tilde{e}_{z,m'}^{i(00)} \right) \\ & \cdot \left( \sin\theta \tilde{e}_{x,m}^{i(00)} + \cos\theta \tilde{e}_{z,m}^{i(00)} \right)^* \end{aligned} \right] \\ & + \frac{2}{g} \left[ \begin{aligned} & \left( \cos\theta \tilde{e}_{x,m'}^{i(00)} - \sin\theta \tilde{e}_{z,m'}^{i(00)} \right) \\ & \cdot \left( \cos\theta \tilde{e}_{x,m}^{i(00)} - \sin\theta \tilde{e}_{z,m}^{i(00)} \right)^* \end{aligned} \right]. \end{aligned} \quad (18)$$

In  $M^{h,h}$ , only TE modes appear. The PMFs in (18) can be simplified according to (12). As such, the low-frequency fundamental-harmonic term yields

$$\begin{aligned} & \frac{2}{g(1-n_\theta^2)} \left[ \begin{aligned} & \left( \sin\theta \tilde{e}_{x,m'}^{(00)} + \cos\theta \tilde{e}_{z,m'}^{(00)} \right) \\ & \cdot \left( \sin\theta \tilde{e}_{x,m}^{(00)} + \cos\theta \tilde{e}_{z,m}^{(00)} \right)^* \end{aligned} \right] \\ & + \frac{2}{g} \left[ \begin{aligned} & \left( \cos\theta \tilde{e}_{x,m'}^{(00)} - \sin\theta \tilde{e}_{z,m'}^{(00)} \right) \\ & \cdot \left( \cos\theta \tilde{e}_{x,m}^{(00)} - \sin\theta \tilde{e}_{z,m}^{(00)} \right)^* \end{aligned} \right], \end{aligned} \quad (19)$$

where the complex conjugate can be removed because  $\tilde{e}_{z,m}^{(00)}$  and  $\tilde{e}_{x,m}^{(00)}$  are real.

In the lower-left matrix quarter  $M^{h,e}$ , only the order  $m'$  corresponds to TE modes, and so the corresponding PMFs can be simplified according to (12). On the other hand,  $m$  is a TM order, therefore the low-frequency simplification (15) is

used. The low-frequency fundamental-harmonic term in  $M^{h,e}$  becomes

$$-\frac{j}{k_m^e} \frac{kn_\theta}{1-n_\theta^2} \frac{2}{g} \left( \sin\theta \tilde{e}_{x,m'}^{(00)} + \cos\theta \tilde{e}_{z,m'}^{(00)} \right) \tilde{e}_{y,m}^{(00)}, \quad (20)$$

where the complex conjugate is removed because  $\tilde{e}_{y,m}^{(00)}$  is real.

Finally, in  $M^{e,e}$ , all orders correspond to TM modes. Given (41), the third and fourth line in (18) vanish. The remaining PMFs can be replaced by the TM simplification (15), leading to a  $(kn_\theta)^2$  factor. The reduced fundamental-harmonic term is

$$\frac{k^2}{k_m^e k_m^e} \frac{n_\theta^2}{1-n_\theta^2} \frac{2}{g} \tilde{e}_{y,m'}^{(00)} \tilde{e}_{y,m}^{(00)}. \quad (21)$$

3) *Higher-harmonic terms:* When  $s \neq 0$  or  $\ell \neq 0$  at low frequency, the vertical spectral function and the harmonic wavenumbers become frequency-independent, according to (11) and (9), respectively. Then, the low-frequency higher-harmonic terms in (7) yield

$$\lim_{k \rightarrow 0} \bar{f}^{(s\ell)} \left[ \begin{aligned} & k^2 \left( \tilde{e}_{x,m'}^{i(s\ell)} \tilde{e}_{x,m}^{i(s\ell)*} + \tilde{e}_{z,m'}^{i(s\ell)} \tilde{e}_{z,m}^{i(s\ell)*} \right) \\ & - \left( \frac{s2\pi}{p_z} \tilde{e}_{x,m'}^{i(s\ell)} - \frac{\ell 2\pi}{p_x} \tilde{e}_{z,m'}^{i(s\ell)} \right) \\ & \cdot \left( \frac{s2\pi}{p_z} \tilde{e}_{x,m}^{i(s\ell)} - \frac{\ell 2\pi}{p_x} \tilde{e}_{z,m}^{i(s\ell)} \right)^* \end{aligned} \right]. \quad (22)$$

In  $M^{h,h}$ , when  $k \rightarrow 0$ , the first line in (22) vanishes. As such, given (12), its higher-harmonic terms are reduced to

$$-\bar{f}^{(s\ell)} \left[ \begin{aligned} & \left( \frac{s2\pi}{p_z} \tilde{e}_{x,m'}^{(s\ell)} - \frac{\ell 2\pi}{p_x} \tilde{e}_{z,m'}^{(s\ell)} \right) \\ & \cdot \left( \frac{s2\pi}{p_z} \tilde{e}_{x,m}^{(s\ell)} - \frac{\ell 2\pi}{p_x} \tilde{e}_{z,m}^{(s\ell)} \right)^* \end{aligned} \right]. \quad (23)$$

On the other hand, in  $M^{e,e}$ ,  $m'$  and  $m$  are TM orders. Therefore, the cartesian components of the PMFs satisfy (41), meaning that the second and third line in (22) vanish. Keeping in mind that in  $M^{e,e}$ , the harmonic terms are summed to the diagonal term defined in (17) – which is proportional to  $k^2$  – the first line of (22) is not dismissed at  $k \rightarrow 0$ . Therefore the reduced higher-harmonic terms are

$$\frac{k^2}{k_m^e k_m^e} \bar{f}^{(s\ell)} \Gamma^{(s\ell)^2} \tilde{e}_{y,m'}^{(s\ell)} \left[ \tilde{e}_{y,m}^{(s\ell)} \right]^*. \quad (24)$$

Finally, in  $M^{h,e}$ , the second and third line of (22) vanish as in  $M^{e,e}$ , because  $m$  is a TM order. The remaining  $k^2$ -proportional terms are dismissed, because there are no diagonal terms in  $M^{h,e}$ . Consequently, higher-harmonic terms of  $M^{h,e}$  completely vanish at low frequency.

### D. Low-frequency dispersion matrix

Considering the simplifications of the previous paragraphs, the total low-frequency dispersion matrix can be written as

$$\left[ \begin{aligned} & k^2 \left( \Sigma^e + \frac{n_\theta^2}{1-n_\theta^2} \frac{2}{g} \mathbf{u}^e [\mathbf{u}^e]^H \right) & jk \frac{n_\theta}{1-n_\theta^2} \frac{2}{g} \mathbf{u}^e [\mathbf{u}^h]^H \\ & -jk \frac{n_\theta}{1-n_\theta^2} \frac{2}{g} \mathbf{u}^h [\mathbf{u}^e]^H & \Sigma^h + \frac{1}{1-n_\theta^2} \frac{2}{g} \mathbf{u}^h [\mathbf{u}^h]^H \end{aligned} \right], \quad (25)$$

where  $\cdot^H$  designates the conjugate transpose of the vectors. In the matrix (25), according to (16), (21), and (24),

$$(\Sigma^e)_{m'm} = -\delta_{mm'} \epsilon_r p_x p_z I_m^e \frac{\coth(hk_m^e)}{k_m^e} + \sum_{\ell, s \neq (0,0)} \bar{f}^{(s\ell)} \frac{\Gamma^{(s\ell)^2}}{k_{m'}^e k_m^e} \bar{e}_{y,m'}^{(s\ell)} \left[ \bar{e}_{y,m}^{(s\ell)} \right]^*, \quad (26)$$

$$\text{and } u_m^e = \frac{1}{k_m^e} \bar{e}_{y,m}^{(00)}, \quad (27)$$

and, according to (17), (19), and (23),

$$(\Sigma^h)_{m'm} = \delta_{mm'} \frac{p_x p_z}{\mu_r} I_m^h k_m^h \coth(hk_m^h) + \frac{2}{g} \left[ \begin{array}{c} \left( \cos \theta \bar{e}_{x,m'}^{(00)} - \sin \theta \bar{e}_{z,m'}^{(00)} \right) \\ \cdot \left( \cos \theta \bar{e}_{x,m}^{(00)} - \sin \theta \bar{e}_{z,m}^{(00)} \right)^* \end{array} \right] - \sum_{\ell, s \neq (0,0)} \bar{f}^{(s\ell)} \left[ \begin{array}{c} \left( \frac{s2\pi}{p_z} \bar{e}_{x,m'}^{(s\ell)} - \frac{\ell 2\pi}{p_x} \bar{e}_{z,m'}^{(s\ell)} \right) \\ \cdot \left( \frac{s2\pi}{p_z} \bar{e}_{x,m}^{(s\ell)} - \frac{\ell 2\pi}{p_x} \bar{e}_{z,m}^{(s\ell)} \right)^* \end{array} \right], \quad (28)$$

$$\text{and } u_m^h = \sin \theta \bar{e}_{x,m}^{(00)} + \cos \theta \bar{e}_{z,m}^{(00)}. \quad (29)$$

The low-frequency Fourier transforms of the electric field are defined in (12), (14) and (15):  $\bar{e}_{z,m}^{(s\ell)}$  and  $\bar{e}_{x,m}^{(s\ell)}$  correspond to transverse TE modes,  $\bar{e}_{y,m}^{(s\ell)}$  to the longitudinal TM field. The squared TM norm  $I_m^e$  can be expressed as a function of the longitudinal modal function  $e_{y,m}$  according to (36), such that the transverse fields need not be computed.

Each coefficient  $u_m^e$  can be interpreted as the average of the longitudinal electric field component for a TM mode of order  $m$ , whereas  $u_m^h$  is the norm of the projection of the average transverse TE field onto the propagation direction.

### E. Closed-form solution of the dispersion equation

Given the dispersion equation (6), the determinant of the matrix (25) must be null. This implies that  $kn_\theta$  can be factored out of the first row and of the first column of the dispersion matrix. Additionally,  $(1 - n_\theta^2)$  is multiplied to the whole matrix. The resulting low-frequency dispersion equation can be written as

$$\left| (1 - n_\theta^2) \begin{bmatrix} \frac{1}{n_\theta^2} \Sigma^e & \mathbf{0} \\ \mathbf{0} & \Sigma^h \end{bmatrix} + \frac{2}{g} \begin{bmatrix} \mathbf{j} \mathbf{u}^e \\ \mathbf{u}^h \end{bmatrix} \begin{bmatrix} \mathbf{j} \mathbf{u}^e \\ \mathbf{u}^h \end{bmatrix}^H \right| = 0. \quad (30)$$

The determinant involved in (30) applies to the sum of a rank-2 matrix with a diagonal matrix that is assumed to be invertible. As such, this determinant can be reformulated using the determinant lemma [49, p. 416], which states that

$$|\Sigma + \mathbf{u} \mathbf{v}^H| = (1 + \mathbf{v}^H \Sigma^{-1} \mathbf{u}) |\Sigma|, \quad (31)$$

with  $\Sigma$  a square invertible matrix and  $\mathbf{u}$  and  $\mathbf{v}$  vectors of appropriate sizes. Applied to (30), this yields the reformulated scalar dispersion equation

$$1 - n_\theta^2 + \frac{2}{g} \begin{bmatrix} \mathbf{j} \mathbf{u}^e \\ \mathbf{u}^h \end{bmatrix}^H \left[ \begin{array}{cc} \frac{1}{n_\theta^2} \Sigma^e & \mathbf{0} \\ \mathbf{0} & \Sigma^h \end{array} \right]^{-1} \begin{bmatrix} \mathbf{j} \mathbf{u}^e \\ \mathbf{u}^h \end{bmatrix} = 0. \quad (32)$$

After developing the matrix-vector products, this yields

$$1 - n_\theta^2 + n_\theta^2 \frac{2}{g} [\mathbf{u}^e]^H [\Sigma^e]^{-1} \mathbf{u}^e + \frac{2}{g} [\mathbf{u}^h]^H [\Sigma^h]^{-1} \mathbf{u}^h = 0. \quad (33)$$

Expression (33) is a first-order equation of unknown  $n_\theta^2$ . Therefore, a closed-form solution of this equation is found, namely

$$n_\theta = \sqrt{\frac{1 + \frac{2}{g} [\mathbf{u}^h]^H [\Sigma^h]^{-1} \mathbf{u}^h}{1 - \frac{2}{g} [\mathbf{u}^e]^H [\Sigma^e]^{-1} \mathbf{u}^e}}, \quad (34)$$

where  $\Sigma^e$ ,  $\mathbf{u}^e$  and  $\Sigma^h$  and  $\mathbf{u}^h$  are defined in (26), (27), (28) and (29), respectively.

This closed-form formula of the effective refractive index is frequency-independent, and can be computed with only low-frequency information about the PMFs of TE modes, namely the coefficients  $\bar{e}_{z,m}^{(s\ell)}$ ,  $\bar{e}_{x,m}^{(s\ell)}$ , and the longitudinal electric modal functions of TM modes, namely the coefficients  $\bar{e}_{y,m}^{(s\ell)}$ . When analytic expressions of these modal functions are available, the computation of the index can be accelerated by dismissing all the modes whose contributions vanish in (34). Conditions for this dismissal are given in Appendix C. The resulting speeding up of parametric studies will be illustrated with numerical examples in the next section. Additionally, it is shown that this formula is valid over a large bandwidth, despite being computed at low frequency, due to the low-dispersive behavior of GS waveguides.

## IV. NUMERICAL RESULTS

In this section, the closed-form formula of the effective refractive index (34) is applied to two canonical examples of holey GS PPWs: with empty rectangular holes, and with circular holes filled with a dielectric. Both structure are like in Fig. 1, with different hole cross-sections. In Fig. 3a, the holes are rectangular waveguides of size  $a_z \times a_x$ , oriented along the  $z$ - and  $x$ -directions. In Fig. 3b, the holes are circular waveguides of radius  $r$ , filled with a dielectric of relative permittivity  $\epsilon_r$  and relative permeability  $\mu_r = 1$ . In all cases, the metasurfaces have a square grid of unit cells  $p_z = p_x = 4 \text{ mm}$ .

All the terms in the refractive index formula (34) can be derived from the modal functions of the holes, which are known analytically. These modal functions are given in Appendix B, along with all the other related terms, notably the low-frequency coefficients of the PMFs. Because some of these coefficients are zero, it can be shown that the corresponding modes do not contribute to the refractive index in (34), and can thus be dismissed. These dispensable modes are given for rectangular and circular holes at the end of Appendix C.

Once all the terms in (34) are known, the formula can be applied to various geometries and compared to other analysis methods. First, considering rectangular modes, the speed-up of this homogenization method is highlighted through the study of mode convergence. Second, efficient parametric studies are performed, by varying the geometrical parameters of the GS PPW with rectangular holes, and for circular holes filled with different dielectrics. Finally, the bandwidth in which the formula is valid is studied.

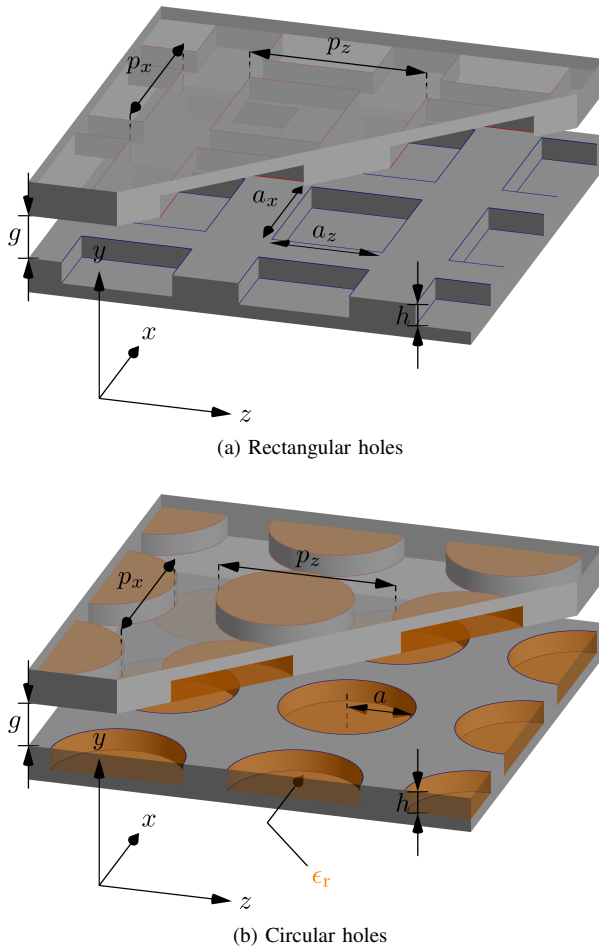


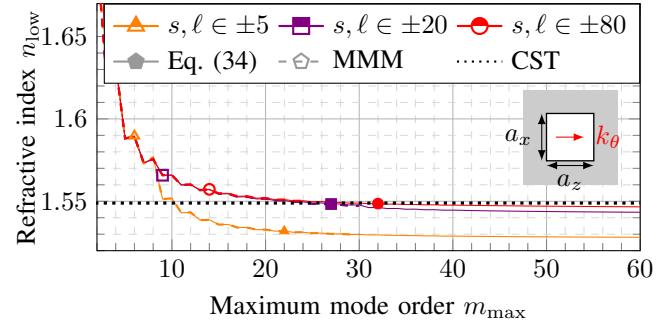
Fig. 3. Holey GS PPWs with canonical hole cross-sections used for numerical results. (a) Empty rectangular holes of size  $a_z \times a_x$ . (b) Circular holes with radius  $a$ , filled with a dielectric of relative permittivity  $\epsilon_r$ .

### A. Rectangular holes: convergence analysis

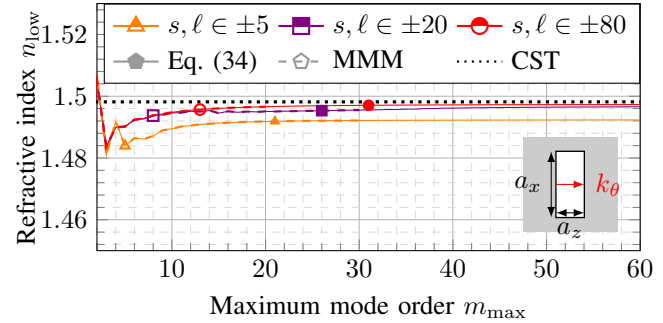
The low-frequency modal terms for rectangular holes (42)-(45) and (48)-(50) are used in the closed-form formula (34) to compute the effective refractive index of the structure for various geometrical parameters. In the MMM formulation in II-B, higher-order harmonics and modes have a reduced impact on the effective wave propagation, and can therefore be truncated, such that the dispersion matrix in (6) has a finite size [39].

However, this truncation depends on geometry and on the desired accuracy. Solving the dispersion equation (6) iteratively can then become prohibitively long, not to say tricky. Indeed, for hundreds of TM and TE modes in the holes, the determinant of the dispersion matrix easily reaches the machine's numerical precision if no specific measures are taken. In the following, instead of solving (6) directly, we consider the log-determinant of the dispersion matrix, and use a golden-section-search [50] to iteratively determine when the log-determinant tends towards  $-\infty$ .

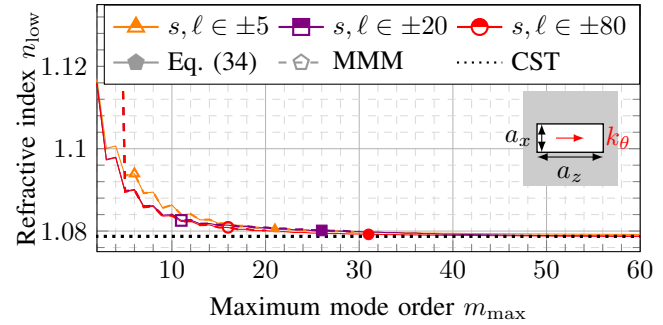
In the following, we study the convergence of the low-frequency refractive index for increasingly many modes. This study is performed with two techniques in parallel. On the one side, by solving the dispersion equation (6) at 1 MHz



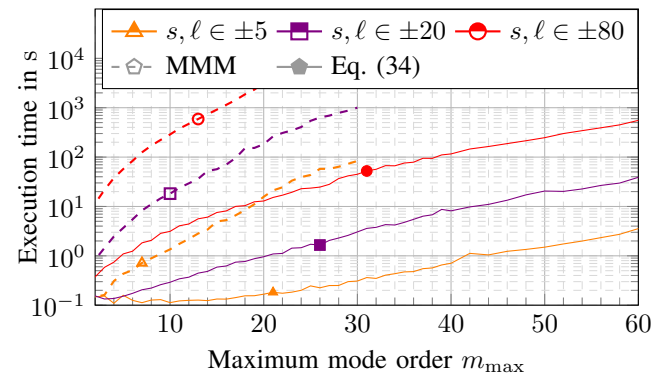
(a)  $g = 0.1$  mm,  $h = 5$  mm,  $a_z = a_x = 3$  mm,  $\theta = 0^\circ$



(b)  $g = 0.1$  mm,  $h = 5$  mm,  $a_z = 1.5$  mm,  $a_x = 3.5$  mm,  $\theta = 0^\circ$



(c)  $g = 0.1$  mm,  $h = 5$  mm,  $a_z = 3.5$  mm,  $a_x = 1.5$  mm,  $\theta = 0^\circ$



(d) Execution time

Fig. 4. Study of the refractive index convergence as the number of modes increases. Each marker shape corresponds to a different number of Floquet harmonics. The structures under study are GS PPWs with rectangular holes, as illustrated in Fig. 3a. The low-frequency refractive index  $n_{low}$  is computed in two ways: the MMM approximation (dashed curves) and the closed-form formula (34) (solid curves). A reference result is also computed with CST, and is indicated by the dotted lined. (a-c) Refractive index as a function of the maximum mode order. (d) Corresponding computation time of each point.



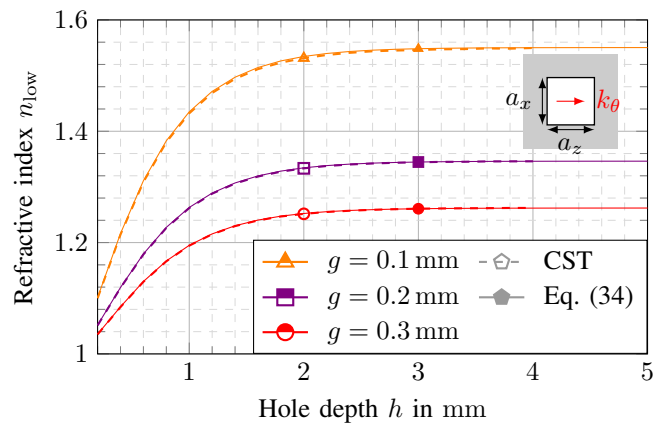
with the use of the log-determinant and a golden-search-technique. We refer to this as the MMM approximation, for which around 20 iterations are performed to obtain an index convergence of  $10^{-5}$ . On the other side, the low-frequency refractive index is computed with the closed-form formula (34). While the precision chosen in this comparison is much higher than the one required for applications, our aim is the rigorous validation of the accuracy of (34). Additionally, a CST simulation validates the convergence value of both methods. Holey GS PPWs with three different holes cross-sections and depth  $h = 5$  mm are considered. The metasurfaces have a periodicity  $p_z = p_x = 4$  mm and are separated by a gap  $g = 0.1$  mm. The waves propagate in the direction  $\theta = 0^\circ$ .

In Figs. 4a-4c, the computed low-frequency refractive index is plotted as a function of the maximum mode order  $m_{\max} = q_{\max}$ . The maximum mode order designates both  $q$  and  $m$ , for both TM and TE modes. As such, the total number of considered modes is  $2m_{\max}(m_{\max} + 1)$  (no  $TE_{00}$ ,  $TM_{q0}$  and  $TM_{0m}$  modes). The highest abscissa point in Fig. 4,  $m_{\max} = 40$ , corresponds to 3280 modes in the square holes. Additionally, each curve corresponds to a different number of Floquet harmonics, where orders  $s$  and  $\ell$  range within  $\pm 5$ ,  $\pm 20$  or  $\pm 80$ . This latter case represents more than 25 000 Floquet harmonics. For each number of harmonics, the average computation time over the three structures is plotted in Fig. 4d.

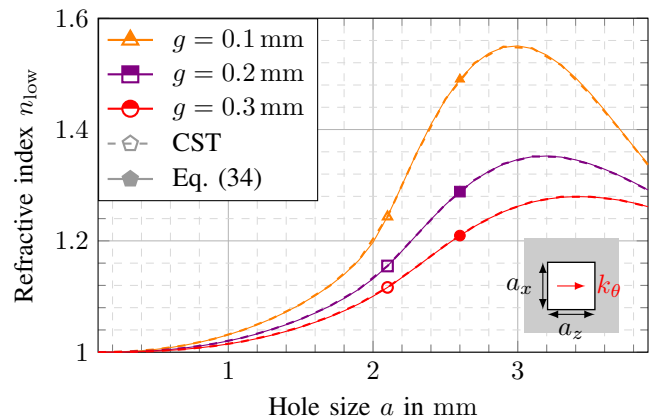
On a computer with a Quad-Core Intel Core i5 @2.4 GHz processor and with 8 GB of RAM, running the algorithms on Matlab without any parallelization effort, the total execution time to obtain the MMM curves up to  $m_{\max} = 20$  for each structure is around 4 hours, whereas the closed-form formula requires only 106 seconds. The higher the number of modes, the higher the disparity in time between the two methods. That is why the MMM approximation was not computed for orders higher than  $m_{\max} = 20$ . In this latter case, with harmonics  $\pm 80$ , the closed-form formula is 250 times faster than the MMM method. There are several reasons for this speed-up. First, the MMM approximation is iterative, and must evaluate the matrix determinant several dozen times, depending on the search interval and the desired accuracy. Second, the low-frequency method developed in this paper enables the dismissal of many modes that have no impact on propagation. As such, for  $2m_{\max}(m_{\max} + 1)$  modes with the MMM approximation, only  $\frac{3}{4}(m_{\max} + 1)^2$  are kept for the closed-form formula, as described in Appendix C. Finally, the matrices in (34) have a much simpler form than the original dispersion matrix, and can be formed in more efficient ways.

On top of the speed of execution, the implementation complexity is an other advantage of the closed-form formula. No iterative root-finding algorithm is involved, and so no parameters such as convergence limit or interval of search must be tuned. Additionally, no matrix determinants are computed, and so there are no problems with machine precision as with the direct MMM method.

For all subsequent numerical results, the number of modes and harmonics is high enough to achieve sufficient convergence of the effective refractive index.



(a)  $p_z = p_x = 4$  mm,  $a = 3$  mm,  $\theta = 0^\circ$



(b)  $p_z = p_x = 4$  mm,  $h = 5$  mm,  $\theta = 0^\circ$

Fig. 5. Parametric study of the low-frequency refractive index for GS PPWs with rectangular holes, as illustrated in Fig. 3a. The low-frequency refractive index  $n_{\text{low}}$  computed with the closed-form formula (34) (solid curves) is compared to CST data (dashed curves). (a) As a function of  $h$ , for different  $g$ ;  $a = 3$  mm. (b) As a function of  $a$ , for different  $g$ ;  $h = 5$  mm.

### B. Rectangular holes: parametric studies

A motivation for a fast analysis method of holey GS PPWs is the cumbersome parametric studies needed for the design of lens antennas. Here, the low-frequency refractive index is computed with the closed-form formula (34) as a function of the structure's dimensions or the propagation direction. In all cases, the GS PPW has cells of size  $p_z = p_x = 4$  mm. All results are compared to CST data, computed for  $k_\theta = 0.4 \text{ m}^{-1}$ , which corresponds to a frequency of approximately 15 MHz.

In Fig. 5, the propagation direction is  $\theta = 0^\circ$ , and the holes are squares of size  $a$ . In each subfigure, the low-frequency refractive index is plotted as a function of a different geometrical parameter: the hole depth  $h$  in 5a, and the hole size in 5b. The parametric curves depend on the gap  $g$ . Fig. 5a shows that beyond a certain depth,  $h$  does not impact the effective refractive index of the holey waveguide. Indeed, the hole's electrical size is tiny, therefore the rectangular waveguide modes are attenuated in the holes. The bottom of the holes barely interacts with the fields if it lies beyond a certain distance. This can be verified by considering the low-frequency matrices  $\Sigma^e$  in (26) and  $\Sigma^h$  in (28), which are the only  $h$ -dependent terms in the refractive index formula (34).

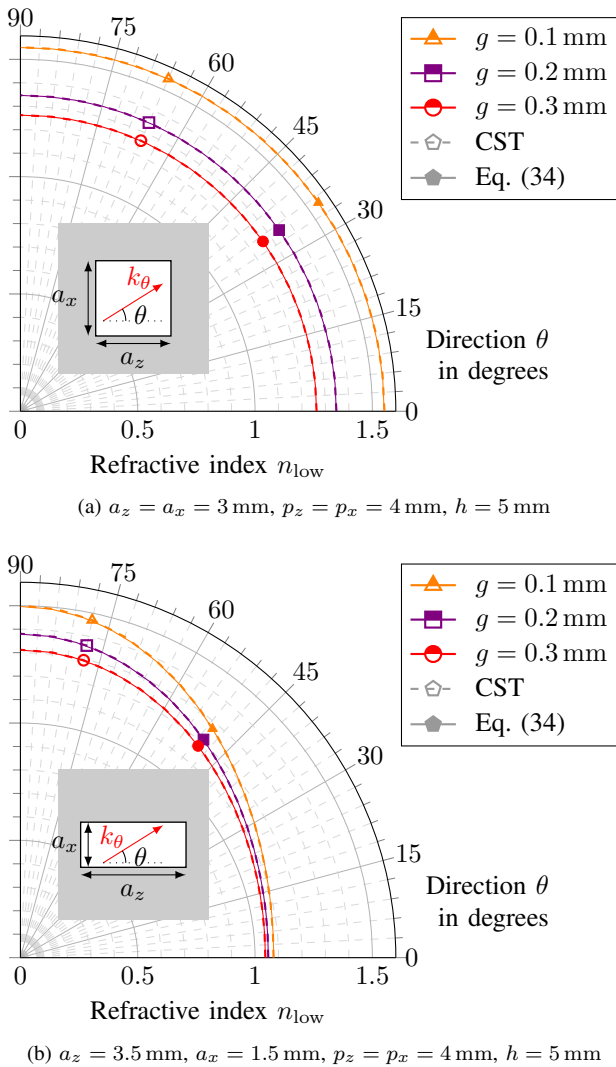


Fig. 6. Study of the low-frequency refractive index as a function of the propagation direction  $\theta$ , for GS PPWs with rectangular holes, as illustrated in Fig. 3a. The low-frequency refractive index  $n_{low}$  is computed with two techniques: CST's eigensolver (dashed curves) and the closed-form formula (34) (solid curves). The latter uses mode orders up to 24 and harmonic orders up to  $\pm 100$ . (a) Square holes with  $a = 3$  mm, for different  $g$ . (b) Rectangular holes with  $a_z = 3.5$  mm and  $a_x = 1.5$  mm, for different  $g$ .

Given  $k_m$  the smallest cut-off wavenumber of the modes in the holes, the term  $\coth(hk_m^i)$  tends towards 1 when  $h$  increases. This behavior does not depend on the hole cross-section. The impact of the hole size in Fig. 5b is more intricate, but a large range of refractive indexes can be achieved by changing the size of the holes. For a Luneburg lens, indexes up to  $\sqrt{2}$  are needed, which is achieved here when  $g = 0.1$  mm.

The closed-form formula (34) is a  $\theta$ -dependent function. As such, it can be used to study the isotropy of the holey GS PPW, by computing the low-frequency refractive index as a function of the propagation direction. This is done in Fig. 6 for two different structures: square holes of size  $a = 3$  mm in Fig. 6a, and rectangular holes with  $a_z = 3.5$  mm and  $a_x = 1.5$  mm in Fig. 6b. The hole depth is fixed at  $h = 5$  mm.

Interestingly, the GS PPW with square holes is isotropic. This might seem counter-intuitive, given that the metasurface is made of a square lattice of holes. As such, the periodicity

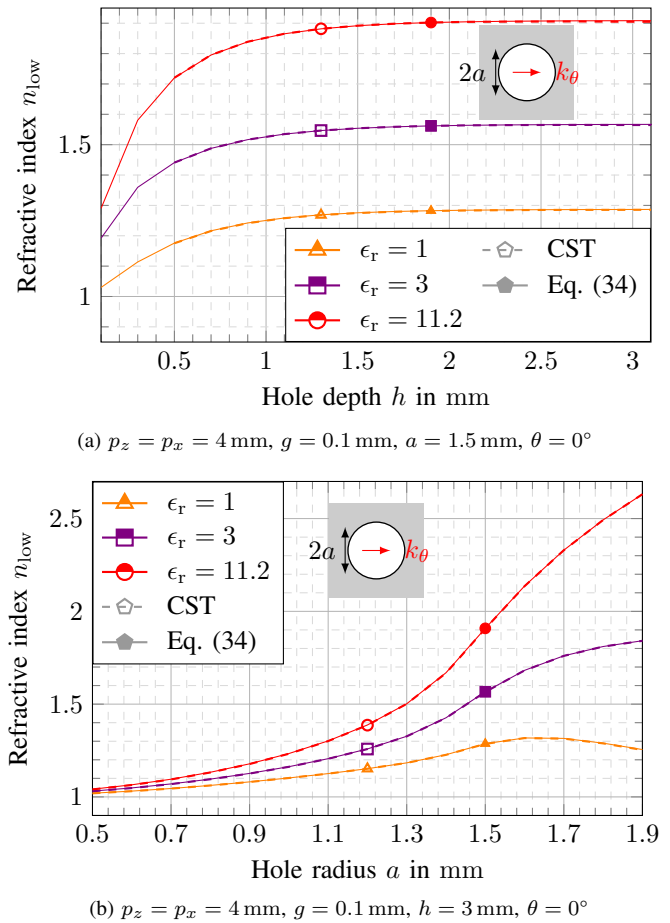


Fig. 7. Parametric study of the low-frequency refractive index for circular holes. The low-frequency refractive index  $n_{low}$  computed with the closed-form formula (34) (solid curves) is compared to CST data (dashed curves). The structure under study is illustrated in Fig. 3b, with  $p_z = p_x = 4$  mm,  $g = 0.1$  mm and different values of  $\epsilon_r$ . (a) For different hole radii  $a$ . (b) For different hole depths  $h$ .

in different directions is not the same. Nevertheless, Fig. 6a displays a constant refractive index as function of the propagation angle. Indeed, a deeper study of the closed-form formula (34) for square holes reveals that the  $\theta$ -dependency vanishes for  $a_z = a_x$ . On the other hand, rectangular holes result in a  $\theta$ -dependent refractive index, as show in Fig. 6b, yielding an anisotropic waveguide. As such, the closed-form index formula (34) enables the fast design of isotropic and anisotropic waveguides, for example for ultra-wideband compressed lenses as illustrated in [27].

### C. Circular holes: parametric studies

In order to illustrate the adaptability of this method to different hole shapes, additional parametric studies are performed for holes with circular cross-section of radius  $a$ , filled with a dielectric material of relative permittivity  $\epsilon_r$ . The modal terms for circular holes (51)-(57) and (60)-(65) are used in the closed-form formula (34) to compute the effective refractive index of the different structures. All results are compared to CST data computed at approximately 15 MHz.

In Fig. 7a the refractive index is plotted as a function of the hole depth  $h$ , and in Fig. 7a it is plotted as a function

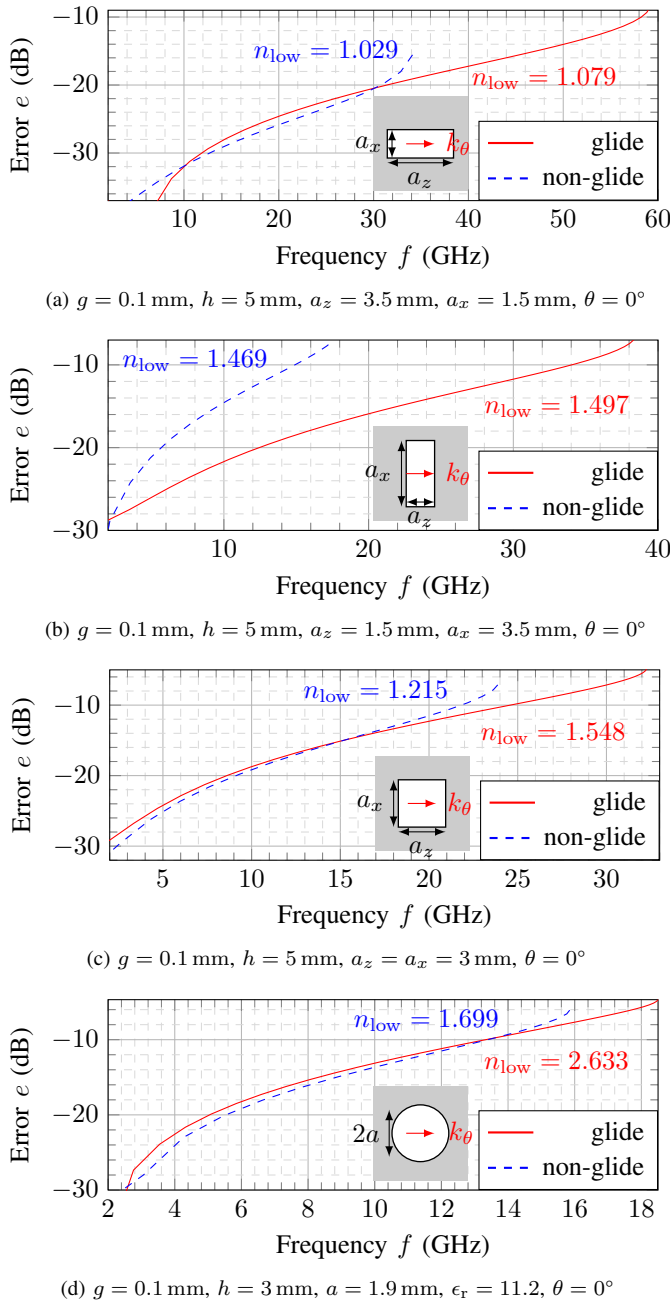


Fig. 8. Error between the low-frequency refractive index  $n_{\text{low}}$  – computed with the closed-form formula (34) – and the refractive index obtained with CST as a function of frequency. The error is normalized and given in dB i.e.,  $e = 10 \log \left| \frac{n(f) - n_{\text{low}}}{n(f)} \right|$ . The propagation direction is  $\theta = 0^\circ$  i.e., along the  $z$ -axis. The refractive indexes are computed for both GS and non-glide holey PPWs, as illustrated in Fig. 3. The holes are rectangular in (a) and (b), square in (c), and circular in (d). All structures have cells of size of  $p_z = p_x = 4$  mm.

of the hole radius  $a$ . Each curve corresponds to a different dielectric filling. As it did for rectangular holes, the closed-form formula matches CST data for all geometries, and for all hole fillings. In practice, circular holes are easier to drill than rectangular holes. The closed-form formula can be used to rapidly manufacture dense waveguides depending on the dielectric material that fills the holes.

#### D. Rectangular and circular holes: wideband validity

Despite being computed in the quasi-static regime, the closed-form formula (34) characterizes holey GS PPWs over a large frequency band, due to the low-dispersive behavior of GS waveguides. In Fig. 8, the low-frequency index  $n_{\text{low}}$  (34) is compared to the refractive index  $n(f)$  computed at higher frequencies  $f$  through the eigenmode solver of CST Studio Suite. The normalized error  $e = 10 \log \left| \frac{n(f) - n_{\text{low}}}{n(f)} \right|$  is plotted as a function of frequency. Different holey GS PPW cases from the parametric studies in Figs. 5 to 7 are considered, along with their non-glide counterpart structures. Indeed, the MMM can also be applied when the upper holes are the reflection of the lower holes with respect to the propagation plane. The resulting matrix equation has the same coefficients as in (7), where only the vertical spectral functions change. The closed-form expression of the non-glide dispersion equation can then be derived following the same steps as for the GS structure.

The analytic low-frequency index  $n_{\text{low}}$  fits the CST results. There remains a relative error at low frequencies, less than a fraction of percent, which can be attributed to the accuracy of the CST meshing: the unit cells of each structures have been decomposed in around 180 thousand mesh cells, but more would be needed to obtain a better accuracy with such a small gap between the plates. This, however, would require simulations lasting several hours or days.

As expected, the validity range of the low-frequency index  $n_{\text{low}}$  is larger in the GS case than for the non-glide structure, due to the low dispersion of GS waveguides and the absence of bandgap between the first and second modes [26]. The frequency validity of the closed-form formula (34) is not inherent to its derivation, but is a consequence of the low-dispersive behavior of holey GS waveguides. These structures have a dispersion curve which is close to linear in the first Brillouin zone [22]. As such, once  $n_{\text{low}}$  is computed, a rough estimate of the frequency validity is given by  $f_{\text{max}} \leq c_0 / (2p_z n_{\text{low}})$ , which corresponds to the frequency at the right-end of the first Brillouin zone i.e.,  $k_z = \pi/p_z$ . Still, this limit presumes a quasi-linear dispersion curve in the first Brillouin zone. Fig. 8 illustrates that when the effective density of the waveguide increases, frequency dispersion is higher, and therefore the accuracy of (34) at  $f_{\text{max}}$  is reduced. If high accuracy is of importance for a given application, the validity of the closed-form formula (34) should be checked with numerical analyses in the band of operation, especially for dense effective media, as (34) does not bear information about the frequency dispersion.

According to the results shown in Fig. 8, the low-frequency index  $n_{\text{low}}$  accurately characterizes the GS waveguide over an ultra-wide band. Tolerating an error of less than 1%, this index can be used up to 31 GHz, 12 GHz, 8 GHz and 7 GHz for the structures in (a), (b) (c) and (d), respectively. If an error of 10% is acceptable, this range rises up to 58 GHz, 34 GHz, 25 GHz and 13 GHz. As expected, the larger the effective refractive index, the smaller the valid frequency range.

## V. CONCLUSION

The low-frequency behavior of holey GS waveguides is studied. By simplifying the dispersion equation derived by means of the MMM, a closed-form formula of the refractive index is found at low frequency. This formula can be adapted to any GS PPW with holes of canonical cross-section, following simple steps:

- 1) Compile the longitudinal TM and transverse TE electric field expressions of the modes that propagate inside the hole, together with their norms, their cut-off wavenumbers, and their Fourier transforms.
- 2) Retain the low-frequency values of these Fourier transforms.
- 3) Eliminate all modes which do not impact low-frequency propagation, as illustrated in Appendix C.
- 4) Insert the remaining terms in the closed-form formula (34) for the refractive index.

Compared to previous numerical or semi-analytic methods:

- The refractive index can be computed analytically for various geometries and cross-sections. No iterative process is needed.
- The low-frequency approach makes it easier to find out which modes have an impact and which are dispensable: as such, dismissing these modes considerably accelerates computations.
- Applying the closed-form formula is much faster than any existing technique, to the point where it enables an accuracy that could previously only be obtained after hours or even days of computations.
- A closed-form formula gives a better physical insight into the influence of some parameters. For square holes, it can be shown that there is no angular dependency, proving the isotropy of such structures.

Therefore, the closed-form formula derived in this paper is a powerful tool for this design of microwave devices such as lens antennas. For non-canonical hole cross-sections, whose modal functions are not known analytically, the formula can be associated to a two-dimensional finite element method in order to compute the eigensolutions of the holes.

## APPENDIX A

### LOW-FREQUENCY REDUCTION OF TM PMFs

Here, we derive the properties of TM modes that are used in III to simplify the dispersion matrix at low frequency. According to cylindrical waveguide field theory [48, p. 100], the transverse modal functions of TM modes can be related to the longitudinal electric field component  $e_{y,m}$  with

$$\mathbf{e}_{t,m}^e(z, x) = \begin{bmatrix} e_{z,m}^e(z, x) \\ e_{x,m}^e(z, x) \end{bmatrix} = \frac{1}{k_m^e} \nabla_t e_{y,m}(z, x), \quad (35)$$

such that both transverse and longitudinal modal functions are real and frequency-independent. Thereby, the squared norm of TM modes (4) can be expressed as a function of  $e_{y,m}$  as

$$I_m^e = \frac{1}{k_m^e{}^2} \iint_S \nabla_t e_{y,m}(z, x) \cdot \nabla_t e_{y,m}(z, x) ds. \quad (36)$$

From Green's theorem [51, p. 431], it can be shown that

$$\iint_S \nabla_t e_{y,m}(z, x) dz dx = \int_{\partial S} e_{y,m}(z, x) \mathbf{n} dl, \quad (37)$$

where  $\partial S$  is the hole contour and  $\mathbf{n}$  is the exterior normal at each contour point. Given this result, the PMF defined in (5) is then equal to

$$\tilde{e}_{t,m}^{e(s\ell)} = \iint_S \left[ \nabla_t \left\{ \frac{e_{y,m}}{k_m^e} F^{(s\ell)} \right\} - \frac{e_{y,m}}{k_m^e} \nabla_t \left\{ F^{(s\ell)} \right\} \right] ds \quad (38)$$

$$= \oint_{\partial S} \frac{e_{y,m}}{k_m^e} F^{(s\ell)} \mathbf{n} dl + j \begin{bmatrix} k_z^{(s)} \\ k_x^{(\ell)} \end{bmatrix} \iint_S \frac{e_{y,m}}{k_m^e} F^{(s\ell)} ds \quad (39)$$

$$= \frac{j}{k_m^e} \begin{bmatrix} k_z^{(s)} \\ k_x^{(\ell)} \end{bmatrix} \iint_S e_{y,m} F^{(s\ell)} ds, \quad (40)$$

where the last line is obtained considering that the longitudinal electric field vanishes on the hole contour. Therefore,

$$\begin{cases} k_x^{(\ell)} \tilde{e}_{z,m}^{e(s\ell)} = k_z^{(s)} \tilde{e}_{x,m}^{e(s\ell)} & \text{in general,} \\ \sin \theta \tilde{e}_{z,m}^{e(00)} = \cos \theta \tilde{e}_{x,m}^{e(00)} & \text{for } s = \ell = 0, \end{cases} \quad (41)$$

where (1) is used in the case of the fundamental harmonic to introduce the propagation angle  $\theta$ . Equations (41) are true for all TM modes, whatever the cross-section of the holes.

## APPENDIX B

### PROJECTED MODAL FUNCTIONS EXAMPLES

In Section IV, the low-frequency effective refractive indexes of GS PPWs with rectangular and circular holes are computed with the closed-form formula (34). This formula is a function of the low-frequency PMFs of the holes. In this appendix, these PMFs are computed and reduced in the limit  $(k_z, k_x) \rightarrow (0, 0)$ .

#### A. Rectangular holes

The GS PPW with rectangular holes presented in Fig. 3a is considered. Rectangular waveguide modes are derived in [48, p. 117]. Each mode depends on a pair of orders  $(q, m)$ . The cut-off frequencies of both TM and TE modes are

$$k_{qm} = \sqrt{\left(\frac{m\pi}{a_z}\right)^2 + \left(\frac{q\pi}{a_x}\right)^2}. \quad (42)$$

For propagation in the  $y$ -direction, the longitudinal TM modal functions are

$$e_{y,qm}(z, x) = \sin\left(\frac{m\pi}{a_z} z\right) \sin\left(\frac{q\pi}{a_x} x\right), \quad (43)$$

with both mode orders  $q > 0$  and  $m > 0$ . The transverse modal functions in the TE case are

$$\mathbf{e}_{t,qm}^h = \begin{bmatrix} \frac{q\pi}{a_x k_{qm}} \cos\left(\frac{m\pi}{a_z} z\right) \sin\left(\frac{q\pi}{a_x} x\right) \\ -\frac{m\pi}{a_z k_{qm}} \sin\left(\frac{m\pi}{a_z} z\right) \cos\left(\frac{q\pi}{a_x} x\right) \end{bmatrix}, \quad (44)$$

where  $(q, m) \neq (0, 0)$ . The vectors are given along the cartesian coordinates  $(z, x)$ .

From (4), the norms of both TM and TE modes are

$$I_{qm} = \frac{1}{k_{qm}^2} \frac{\pi^2}{2^{1+\min(1,q,m)}} \left( \frac{a_x}{a_z} m^2 + \frac{a_z}{a_x} q^2 \right). \quad (45)$$

For TE modes, the PMFs of (44) are computed according to (5). Introducing

$$\zeta_m^z(k) = \frac{1 - (-1)^m e^{-jk a_z}}{\left(\frac{m\pi}{a_z}\right)^2 - k^2}, \quad (46)$$

the PMFs are

$$\vec{e}_{qm}^{h(s\ell)} = \begin{bmatrix} -h(s\ell) \\ e_{z,qm}^{(s\ell)} \\ e_{x,qm}^{(s\ell)} \end{bmatrix} = \begin{bmatrix} \frac{j\pi^2 q^2}{a_x^2} \frac{k_z^{(s)}}{k_{qm}} \zeta_m^z(k^{(s)}) \zeta_q^x(k^{(s)}) \\ \frac{\pi^2 m^2}{j a_z^2} \frac{k_x^{(\ell)}}{k_{qm}} \zeta_m^z(k^{(s)}) \zeta_q^x(k^{(\ell)}) \end{bmatrix}, \quad (47)$$

leading to the low-frequency coefficients defined in (12)

$$\bar{e}_{z,qm}^{(s\ell)} = \begin{cases} \frac{j2\pi^3 s q^2}{k_{qm} p_z a_x^2} \zeta_m^z\left(\frac{s2\pi}{p_z}\right) \zeta_q^x\left(\frac{\ell 2\pi}{p_x}\right) & \text{if } s \neq 0 \text{ or } m \neq 0, \\ \frac{\pi q a_z}{a_x} \zeta_q^x\left(\frac{\ell 2\pi}{p_x}\right) & \text{if } s = m = 0, \end{cases} \quad (48)$$

$$\bar{e}_{x,qm}^{(s\ell)} = \begin{cases} \frac{2\pi^3 \ell m^2}{j k_{qm} p_x a_z^2} \zeta_m^z\left(\frac{s2\pi}{p_z}\right) \zeta_q^x\left(\frac{\ell 2\pi}{p_x}\right) & \text{if } \ell \neq 0 \text{ or } q \neq 0, \\ \frac{-\pi m a_x}{a_z} \zeta_m^z\left(\frac{s2\pi}{p_z}\right) & \text{if } \ell = q = 0. \end{cases} \quad (49)$$

Similarly, for the TM modes (43), the low-frequency coefficients are computed for any  $(s, \ell)$  according to (13) as

$$\bar{e}_{y,qm}^{(s\ell)} = \frac{q m \pi^2}{a_z a_x} \zeta_m^z\left(\frac{s2\pi}{p_z}\right) \zeta_q^x\left(\frac{\ell 2\pi}{p_x}\right). \quad (50)$$

### B. Circular holes

The GS PPW with circular holes presented in Fig. 3b is considered. Circular waveguide modes are derived in [48, pp. 124-126]. Each mode depends on three positive integers  $(q, m, t)$ , standing for the  $m^{\text{th}}$  root  $p_{qm}$  of the  $q^{\text{th}}$  Bessel function of first kind  $J_q$ , or for the  $m^{\text{th}}$  root  $p'_{qm}$  of its derivative  $J'_q$ . The third order  $t = 1, 2$  designates whether the mode has a cosine or sine azimuthal profile. For both TM and TE modes,  $q > 0$  and  $m > 0$  for  $t = 1$ , and  $m > 0$  for  $t = 2$ . The cut-off frequencies  $k_{qm}$  and  $k'_{qm}$  of TM and TE modes are

$$k_{qm} = \frac{p_{qm}}{a} \quad \text{and} \quad k'_{qm} = \frac{p'_{qm}}{a}. \quad (51)$$

A cylindrical coordinate system  $(\rho, \phi)$  is placed at the center of the hole cross-section. For propagation in the  $y$ -direction, the longitudinal TM modal functions are

$$e_{y,qm1}(\rho, \phi) = \sin(q\phi) J_q(k_{qm}\rho) \quad (52)$$

$$\text{and} \quad e_{y,qm2}(\rho, \phi) = \cos(q\phi) J_q(k_{qm}\rho). \quad (53)$$

On the other hand, the modal functions in the TE case in cylindrical coordinates are

$$\begin{bmatrix} e_{\rho,qm1}^h \\ e_{\phi,qm1}^h \end{bmatrix} = \begin{bmatrix} -\cos(q\phi) \frac{q}{k'_{qm}\rho} J_q(k'_{qm}\rho) \\ \sin(q\phi) J'_q(k'_{qm}\rho) \end{bmatrix} \quad (54)$$

$$\text{and} \quad \begin{bmatrix} e_{\rho,qm2}^h \\ e_{\phi,qm2}^h \end{bmatrix} = \begin{bmatrix} \sin(q\phi) \frac{q}{k'_{qm}\rho} J_q(k'_{qm}\rho) \\ \cos(q\phi) J'_q(k'_{qm}\rho) \end{bmatrix}. \quad (55)$$

From (4), the norm of these modes are

$$I_{qm}^e = \frac{\pi a^2}{2^{\min(1,q)}} J_q'^2(p_{qm}), \quad (56)$$

$$\text{and} \quad I_{qm}^h = -\frac{\pi a^2}{2^{\min(1,q)}} J_q(p'_{qm}) J_q''(p'_{qm}). \quad (57)$$

The PMFs of (52), (53), (54) and (55) are computed in cartesian coordinates according to (5). Introducing

$$\mathcal{C}_q^{(s\ell)} = \cos\left(q \operatorname{atan}\left[\frac{\ell p_z}{s p_x}\right]\right), \quad \mathcal{S}_q^{(s\ell)} = \sin\left(q \operatorname{atan}\left[\frac{\ell p_z}{s p_x}\right]\right), \quad (58)$$

$$\text{and} \quad \mathcal{J}_{(\alpha)} = \Gamma^{(s\ell)} J_{q+\alpha}(p'_{qm}) J_q\left(\Gamma^{(s\ell)} a\right) - k'_{qm} J_q(p'_{qm}) J_{q+\alpha}\left(\Gamma^{(s\ell)} a\right), \quad (59)$$

where it is reminded that  $\Gamma^{(s\ell)} = \sqrt{(s2\pi/p_z)^2 + (\ell 2\pi/p_x)^2}$ , then the low-frequency PMFs of the TE modes are

$$\bar{e}_{z,qm1}^{(s\ell)} = \frac{\pi a (-j)^{q-1}}{k_{qm}^2 - \Gamma^{(s\ell)2}} \left[ \mathcal{C}_{q-1}^{(s\ell)} \mathcal{J}_{(-1)} + \mathcal{C}_{q+1}^{(s\ell)} \mathcal{J}_{(1)} \right], \quad (60)$$

$$\bar{e}_{z,qm2}^{(s\ell)} = \frac{\pi a (-j)^{q-1}}{k_{qm}^2 - \Gamma^{(s\ell)2}} \left[ \mathcal{S}_{q-1}^{(s\ell)} \mathcal{J}_{(-1)} + \mathcal{S}_{q+1}^{(s\ell)} \mathcal{J}_{(1)} \right], \quad (61)$$

$$\bar{e}_{x,qm1}^{(s\ell)} = \frac{\pi a (-j)^{q-1}}{k_{qm}^2 - \Gamma^{(s\ell)2}} \left[ \mathcal{S}_{q+1}^{(s\ell)} \mathcal{J}_{(1)} - \mathcal{S}_{q-1}^{(s\ell)} \mathcal{J}_{(-1)} \right], \quad (62)$$

$$\bar{e}_{x,qm2}^{(s\ell)} = \frac{\pi a (-j)^{q-1}}{k_{qm}^2 - \Gamma^{(s\ell)2}} \left[ \mathcal{C}_{q+1}^{(s\ell)} \mathcal{J}_{(1)} - \mathcal{C}_{q-1}^{(s\ell)} \mathcal{J}_{(-1)} \right]. \quad (63)$$

For the TM modes (52) and (53), the low-frequency coefficients are computed for any  $(s, \ell)$  according to (13) as

$$\bar{e}_{y,qm1}^{(s\ell)} = \frac{2\pi p_{qm}}{j^q} \frac{J'_q(p_{qm}) J_q(\Gamma^{(s\ell)} a)}{\Gamma^{(s\ell)2} - k_{qm}^2} \mathcal{S}_q^{(s\ell)}, \quad (64)$$

$$\bar{e}_{y,qm2}^{(s\ell)} = \frac{2\pi p_{qm}}{j^q} \frac{J'_q(p_{qm}) J_q(\Gamma^{(s\ell)} a)}{\Gamma^{(s\ell)2} - k_{qm}^2} \mathcal{C}_q^{(s\ell)}. \quad (65)$$

## APPENDIX C DISPENSABLE MODES

Here, we show that the closed-form solution of the refractive index (34) discloses which modes have no influence on low-frequency propagation. A sufficient condition on the PMF of dispensible modes is derived. In the derivation,  $i = e, h$  is used.

When considering the vector  $\mathbf{u}^i$  in the refractive index formula (34), for a given order  $m$ , if  $u_m^i = 0$ , then all inverse matrix coefficients  $(\Sigma^i)_{m'm}^{-1}$  disappear from (34). However, this is not enough to completely dismiss the corresponding  $m^{\text{th}}$  mode. Indeed, other coefficients of  $(\Sigma^i)^{-1}$  may be dependent on the  $m^{\text{th}}$  mode, due to the inverse operation. Nevertheless, there is a sufficient condition for this mode to be dispensible.

Let  $\mathcal{M}_0$  be the set of all orders  $m_0$  that are dispensible. Let  $\mathcal{M}_1$  be the remaining orders  $m_1$  of modes that are kept. A sufficient condition for a mode  $m_0$  to belong to  $\mathcal{M}_0$  is

$$u_{m_0}^i = 0, \quad \text{and} \quad \forall m_1 \in \mathcal{M}_1, \quad \Sigma_{m_0 m_1}^i = \Sigma_{m_1 m_0}^i = 0. \quad (66)$$

Condition (66) implies that  $m_0$  is dispensible. Indeed, given that (6) requires the determinant of the dispersion matrix to

be null, the modes can be put in an arbitrary order, meaning that the lines and columns of  $\Sigma^i$  can be permuted at will. As such,  $\Sigma^i$  can be rearranged such that its first rows and columns correspond to orders in  $\mathcal{M}_0$ , whereas the remaining rows and columns correspond to orders in  $\mathcal{M}_1$ . Given the second part of the condition (66), the rearranged matrix is a block diagonal matrix. Therefore, its inverse is made of the inverse of its blocks [52, p. 123], namely

$$(\Sigma^i)^{-1} = \begin{bmatrix} \Sigma_0^i & \mathbf{0} \\ \mathbf{0} & \Sigma_1^i \end{bmatrix}^{-1} = \begin{bmatrix} (\Sigma_0^i)^{-1} & \mathbf{0} \\ \mathbf{0} & (\Sigma_1^i)^{-1} \end{bmatrix}, \quad (67)$$

where  $\Sigma_0^i$  and  $\Sigma_1^i$  are the blocks of  $\Sigma^i$  that relate only to mode orders in  $\mathcal{M}_0$  and  $\mathcal{M}_1$ , respectively. Similarly,  $\mathbf{u}^i$  is divided in two subvectors  $\mathbf{u}_0^i$  and  $\mathbf{u}_1^i$ . Given the first part of the condition (66), the product with  $\mathbf{u}^i$  yields

$$[\mathbf{u}_i]^H [\Sigma^i]^{-1} \mathbf{u}_i = \begin{bmatrix} \mathbf{0} \\ \mathbf{u}_1^i \end{bmatrix}^H \begin{bmatrix} (\Sigma_0^i)^{-1} & \mathbf{0} \\ \mathbf{0} & (\Sigma_1^i)^{-1} \end{bmatrix} \begin{bmatrix} \mathbf{0} \\ \mathbf{u}_1^i \end{bmatrix}. \quad (68)$$

As such, if (66) is satisfied, all modes with orders in  $\mathcal{M}_0$  can be dismissed.

a) *Rectangular holes:* For rectangular holes, (27) and (50) indicate that  $u_{qm}^e = 0$  for all TM modes where either  $q$  or  $m$  is even. All these modes belong to  $\mathcal{M}_0$ , as they satisfy the condition (66). Consequently, they can be dismissed when computing the low-frequency refractive index, keeping only TM modes where both  $q$  and  $m$  are odd.

For TE modes, considering (29),(48) and (49), one must be more careful, because some of the modes where  $u_{qm}^h = 0$  still have an impact on the inverse matrix  $[\Sigma^h]^{-1}$  i.e., they do not satisfy the second part of the condition (66). The full conditions is satisfied only by TE modes where  $q + m$  is even i.e., when  $q$  and  $m$  are both even or both odd.

b) *Circular holes:* In the case of circular holes, according to (27), (64) and (65),  $v_{qmt}^e \neq 0$  only for  $q = 0$  or  $t = 2$ . However, not all the modes where  $q > 0$  or  $t = 1$  satisfy the condition (66). After considering the complete matrix  $\Sigma^e$ , all TM modes with  $t = 1$  are dispensable, as well as the TM modes with  $q$  odd.

Similarly, according to (29) and (60)-(63),  $u_{qmt}^h = 0$  when  $q \neq 1$ . But not all these modes belong to  $\mathcal{M}_0$ : condition (66) is only fully satisfied for TE modes where  $q$  is even. Therefore, all TE modes with  $q$  odd are kept.

## REFERENCES

[1] L. Kong, M. K. Khan, F. Wu, G. Chen, and P. Zeng, "Millimeter-Wave Wireless Communications for IoT-Cloud Supported Autonomous Vehicles: Overview, Design, and Challenges," *IEEE Communications Magazine*, vol. 55, no. 1, pp. 62–68, Jan. 2017.

[2] H. Magsi, A. H. Sodhro, F. A. Chachar, S. A. K. Abro, G. H. Sodhro, and S. Pirbhulal, "Evolution of 5G in Internet of medical things," in *2018 International Conference on Computing, Mathematics and Engineering Technologies (iCoMET)*, Mar. 2018, pp. 1–7.

[3] P. Yang, Y. Xiao, M. Xiao, and S. Li, "6G Wireless Communications: Vision and Potential Techniques," *IEEE Network*, vol. 33, no. 4, pp. 70–75, Jul. 2019.

[4] M. Giordani, M. Polese, M. Mezzavilla, S. Rangan, and M. Zorzi, "Toward 6G Networks: Use Cases and Technologies," *IEEE Communications Magazine*, vol. 58, no. 3, pp. 55–61, Mar. 2020.

[5] T. S. Rappaport, S. Sun, R. Mayzus, H. Zhao, Y. Azar, K. Wang, G. N. Wong, J. K. Schulz, M. Samimi, and F. Gutierrez, "Millimeter Wave Mobile Communications for 5G Cellular: It Will Work!" *IEEE Access*, vol. 1, pp. 335–349, 2013.

[6] Y. Wang, J. Li, L. Huang, Y. Jing, A. Georgakopoulos, and P. Demestichas, "5G Mobile: Spectrum Broadening to Higher-Frequency Bands to Support High Data Rates," *IEEE Vehicular Technology Magazine*, vol. 9, no. 3, pp. 39–46, Sep. 2014.

[7] W. Chen, Y. Hsieh, C. Tsai, Y. Chen, C. Chang, and S. Chang, "A compact two-dimensional phased array using grounded coplanar-waveguides butler matrices," in *2012 42nd European Microwave Conference*, Oct. 2012, pp. 747–750.

[8] H. Ren, B. Arigong, M. Zhou, J. Ding, and H. Zhang, "A Novel Design of 4x4 Butler Matrix With Relatively Flexible Phase Differences," *IEEE Antennas and Wireless Propagation Letters*, vol. 15, pp. 1277–1280, 2016.

[9] O. Quevedo-Teruel, M. Ebrahimpouri, and F. Ghasemifard, "Lens Antennas for 5G Communications Systems," *IEEE Communications Magazine*, vol. 56, no. 7, pp. 36–41, Jul. 2018.

[10] B. Fuchs, O. Lafond, S. Rondineau, M. Himdi, and L. L. Coq, "Off-Axis Performances of Half Maxwell Fish-Eye Lens Antennas at 77 GHz," *IEEE Transactions on Antennas and Propagation*, vol. 55, no. 2, pp. 479–482, Feb. 2007.

[11] J. Thornton, D. Smith, S. J. Foti, and Y. Y. Jiang, "Reduced height Luneburg lens antennas for satellite communications-on-the-move," in *2015 Conference on Microwave Techniques (COMITE)*, Apr. 2015, pp. 1–4.

[12] S. Shad and H. Mehrpouyan, "Wideband Beam-Steerable Cylindrical Lens Antenna with Compact Integrated Feed Elements," in *2021 IEEE Radio and Wireless Symposium (RWS)*, Jan. 2021, pp. 14–17.

[13] A. Demetriadou and Y. Hao, "A Grounded Slim Luneburg Lens Antenna Based on Transformation Electromagnetics," *IEEE Antennas and Wireless Propagation Letters*, vol. 10, pp. 1590–1593, 2011.

[14] P.-H. Tichit, S. N. Burokur, D. Germain, and A. de Lustrac, "Design and experimental demonstration of a high-directive emission with transformation optics," *Physical Review B*, vol. 83, no. 15, p. 155108, Apr. 2011.

[15] O. Quevedo-Teruel, H. Chen, A. Díaz-Rubio, G. Gok, A. Grbic, G. Minatti, S. Maci, G. V. Eleftheriades, M. Chen, N. I. Zheludev, N. Papisimakis, S. Choudhury, Z. A. Kudyshev, S. Saha, H. Reddy, A. Boltasseva, V. M. Shalaev, A. V. Kildishev, D. Sievenpiper, C. Caloz, A. Alù, Q. He, L. Zhou, G. Valerio, E. Rajo-Iglesias, Z. Sipus, F. Mesa, R. Rodríguez-Berral, F. Medina, V. Asadchy, S. Tretyakov, and C. Craeye, "Roadmap on metasurfaces," *Journal of Optics*, vol. 21, no. 7, p. 073002, Jul. 2019.

[16] K. Sato and H. Ujiie, "A plate Luneburg lens with the permittivity distribution controlled by hole density," *Electronics and Communications in Japan (Part I: Communications)*, vol. 85, no. 9, pp. 1–12, 2002.

[17] L. Xue and V. F. Fusco, "Printed holey plate Luneburg lens," *Microwave and Optical Technology Letters*, vol. 50, no. 2, pp. 378–380, 2008.

[18] M. Bosiljevac, M. Casaletti, F. Caminita, Z. Sipus, and S. Maci, "Non-Uniform Metasurface Luneburg Lens Antenna Design," *IEEE Transactions on Antennas and Propagation*, vol. 60, no. 9, pp. 4065–4073, Sep. 2012.

[19] J. A. Dockrey, M. J. Lockyear, S. J. Berry, S. A. R. Horsley, J. R. Sambles, and A. P. Hibbins, "Thin metamaterial Luneburg lens for surface waves," *Physical Review B*, vol. 87, no. 12, p. 125137, Mar. 2013.

[20] M. Huang, S. Yang, F. Gao, R. Quarfoth, and D. Sievenpiper, "A 2-D Multibeam Half Maxwell Fish-Eye Lens Antenna Using High Impedance Surfaces," *IEEE Antennas and Wireless Propagation Letters*, vol. 13, pp. 365–368, 2014.

[21] C. D. Diallo, E. Girard, H. Legay, and R. Sauleau, "All-metal Ku-band Luneburg lens antenna based on variable parallel plate spacing Fakir bed of nails," in *2017 11th European Conference on Antennas and Propagation (EUCAP)*, Mar. 2017, pp. 1401–1404.

[22] O. Quevedo-Teruel, M. Ebrahimpouri, and M. N. M. Kehn, "Ultrawideband Metasurface Lenses Based on Off-Shifted Opposite Layers," *IEEE Antennas and Wireless Propagation Letters*, vol. 15, pp. 484–487, Dec. 2016.

[23] P. J. Crepeau and P. R. McIsaac, "Consequences of symmetry in periodic structures," *Proceedings of the IEEE*, vol. 52, no. 1, pp. 33–43, Jan. 1964.

[24] R. Mittra and S. Laxpati, "Propagation in a Wave Guide with Glide Reflection Symmetry," *Canadian Journal of Physics*, vol. 43, no. 2, pp. 353–372, Feb. 1965.

- [25] A. Hessel, M. H. Chen, R. C. M. Li, and A. A. Oliner, "Propagation in periodically loaded waveguides with higher symmetries," *Proceedings of the IEEE*, vol. 61, no. 2, pp. 183–195, Feb. 1973.
- [26] R. Quesada, D. Martín-Cano, F. J. García-Vidal, and J. Bravo-Abad, "Deep-subwavelength negative-index waveguiding enabled by coupled conformal surface plasmons," *Optics Letters*, vol. 39, no. 10, pp. 2990–2993, May 2014.
- [27] M. Ebrahimpouri and O. Quevedo-Teruel, "Ultrawideband Anisotropic Glide-Symmetric Metasurfaces," *IEEE Antennas and Wireless Propagation Letters*, vol. 18, no. 8, pp. 1547–1551, Aug. 2019.
- [28] A. A. Brazález, L. Manholm, M. Johansson, O. Quevedo-Teruel, and J. Miao, "Investigation of a Ka-band Luneburg lens made of a glide-symmetric holey structure," in *2017 International Symposium on Antennas and Propagation (ISAP)*, Oct. 2017, pp. 1–2.
- [29] O. Quevedo-Teruel, J. Miao, M. Mattsson, A. Algaba-Brazalez, M. Johansson, and L. Manholm, "Glide-Symmetric Fully Metallic Luneburg Lens for 5G Communications at Ka-Band," *IEEE Antennas and Wireless Propagation Letters*, vol. 17, no. 9, pp. 1588–1592, Sep. 2018.
- [30] P. Arnberg, O. Barreira Petersson, O. Zetterstrom, F. Ghasemifard, and O. Quevedo-Teruel, "High Refractive Index Electromagnetic Devices in Printed Technology Based on Glide-Symmetric Periodic Structures," *Applied Sciences*, vol. 10, no. 9, p. 3216, Jan. 2020.
- [31] W. Yuan, J. F. Chen, C. Zhang, W. X. Tang, L. Wang, Q. Cheng, and T. J. Cui, "Glide-Symmetric Lens Antenna in Gap Waveguide Technology," *IEEE Transactions on Antennas and Propagation*, vol. 68, no. 4, pp. 2612–2620, Apr. 2020.
- [32] P. Bantavis, P. Bantavis, C. G. Gonzalez, R. Sauleau, G. Goussetis, S. Tubau, and H. Legay, "Broadband graded index Gutman lens with a wide field of view utilizing artificial dielectrics: A design methodology," *Optics Express*, vol. 28, no. 10, pp. 14 648–14 661, May 2020.
- [33] Q. Chen, F. Giusti, G. Valerio, F. Mesa, and O. Quevedo-Teruel, "Anisotropic glide-symmetric substrate-integrated-hole metasurface for a compressed ultrawideband Luneburg lens," *Applied Physics Letters*, vol. 118, no. 8, p. 084102, Feb. 2021.
- [34] F. J. Garcia-Vidal, L. Martín-Moreno, and J. B. Pendry, "Surfaces with holes in them: New plasmonic metamaterials," *Journal of Optics A: Pure and Applied Optics*, vol. 7, no. 2, pp. S97–S101, Jan. 2005.
- [35] M. Bosiljevac, Z. Sipus, and P.-S. Kildal, "Construction of Green's functions of parallel plates with periodic texture with application to gap waveguides – a plane-wave spectral-domain approach," *IET Microwaves, Antennas & Propagation*, vol. 4, no. 11, p. 1799, Jan. 2010.
- [36] F. Mesa, R. Rodríguez-Berral, and F. Medina, "Considerations on the Usage of Transmission Matrices to Study the Dispersion Behavior of Glide-Symmetry Structures," in *2019 13th European Conference on Antennas and Propagation (EuCAP)*, Mar. 2019, pp. 1–4.
- [37] G. Valerio, Z. Sipus, A. Grbic, and O. Quevedo-Teruel, "Accurate Equivalent-Circuit Descriptions of Thin Glide-Symmetric Corrugated Metasurfaces," *IEEE Transactions on Antennas and Propagation*, vol. 65, no. 5, pp. 2695–2700, May 2017.
- [38] B. A. Mouris, A. Fernández-Prieto, R. Thobaben, J. Martel, F. Mesa, and O. Quevedo-Teruel, "On the Increment of the Bandwidth of Mushroom-Type EBG Structures With Glide Symmetry," *IEEE Transactions on Microwave Theory and Techniques*, vol. 68, no. 4, pp. 1365–1375, Apr. 2020.
- [39] M. Bagheriasl, O. Quevedo-Teruel, and G. Valerio, "Bloch Analysis of Artificial Lines and Surfaces Exhibiting Glide Symmetry," *IEEE Transactions on Microwave Theory and Techniques*, vol. 67, no. 7, pp. 2618–2628, Jul. 2019.
- [40] Q. Chen, F. Mesa, P. Padilla, X. Yin, and O. Quevedo-Teruel, "Efficient Leaky-Lens Antenna at 60 GHz Based on a Substrate-Integrated-Holey Metasurface," *IEEE Transactions on Antennas and Propagation*, pp. 1–1, 2020.
- [41] Q. Chen, F. Mesa, X. Yin, and O. Quevedo-Teruel, "Accurate Characterization and Design Guidelines of Glide-Symmetric Holey EBG," *IEEE Transactions on Microwave Theory and Techniques*, pp. 1–1, 2020.
- [42] A. Alex-Amor, A. Palomares-Caballero, F. Mesa, O. Quevedo-Teruel, and P. Padilla, "Dispersion Analysis of Periodic Structures in Anisotropic Media: Application to Liquid Crystals," *arXiv:2007.07648 [physics]*, Jul. 2020.
- [43] G. Valerio, F. Ghasemifard, Z. Sipus, and O. Quevedo-Teruel, "Glide-Symmetric All-Metal Holey Metasurfaces for Low-Dispersive Artificial Materials: Modeling and Properties," *IEEE Transactions on Microwave Theory and Techniques*, vol. 66, no. 7, pp. 3210–3223, Jul. 2018.
- [44] F. Ghasemifard, M. Norgren, O. Quevedo-Teruel, and G. Valerio, "Analyzing Glide-Symmetric Holey Metasurfaces Using a Generalized Floquet Theorem," *IEEE Access*, vol. 6, pp. 71 743–71 750, Nov. 2018.
- [45] A. Alex-Amor, G. Valerio, F. Ghasemifard, F. Mesa, P. Padilla, J. M. Fernández-González, and O. Quevedo-Teruel, "Wave Propagation in Periodic Metallic Structures with Equilateral Triangular Holes," *Applied Sciences*, vol. 10, no. 5, p. 1600, Jan. 2020.
- [46] A. Alex-Amor, F. Ghasemifard, G. Valerio, M. Ebrahimpouri, P. Padilla, J. M. F. González, and O. Quevedo-Teruel, "Glide-Symmetric Metallic Structures With Elliptical Holes for Lens Compression," *IEEE Transactions on Microwave Theory and Techniques*, vol. 68, no. 10, pp. 4236–4248, Oct. 2020.
- [47] R. E. Collin, *Field Theory of Guided Waves*, 2nd ed., ser. The IEEE/OUP Series on Electromagnetic Wave Theory. New York, NY: Inst. of Electrical and Electronics Engineers, 1991.
- [48] D. M. Pozar, *Microwave Engineering*, 4th ed. Hoboken, NJ: John Wiley & Sons, Dec. 2011.
- [49] D. A. Harville, *Matrix Algebra from a Statistician's Perspective*. New York: Springer, 1997.
- [50] J. Kiefer, "Sequential Minimax Search for a Maximum," *Proceedings of the American Mathematical Society*, vol. 4, no. 3, pp. 502–506, 1953.
- [51] J. E. Marsden and A. Tromba, *Vector Calculus*, 6th ed. New York: W.H. Freeman and Company, 2012.
- [52] C. D. Meyer, *Matrix Analysis and Applied Linear Algebra*, 1st ed. Philadelphia, Pennsylvania, USA: Society for Industrial and Applied Mathematics, 2000.



**Boris Fischer** received the M.Sc. degree with high distinction in electrical engineering and information technology at the Technische Universität München, Munich, Germany, in 2019. He is currently pursuing the Ph.D. degree at the Laboratoire Génie Electrique et Electronique de Paris, Sorbonne Université, Paris, France.

His current research is focused on wave propagation in periodic structures at millimeter waves and dispersion of higher-symmetric waveguides made of metallic metasurfaces.

In 2022, he was a co-author of the paper awarded with the Best Student Paper Award at the 16th European Conference on Antennas and Propagation, Madrid, Spain, and he was a finalist for the Best Electromagnetics Paper at the same conference.



**Guido Valerio** (S'06–M'10–SM'18) received the M.S. degree (cum laude and honorable mention) in electronic engineering in 2005, and the Ph.D. degree in electromagnetics in 2009, from La Sapienza University, Rome, Italy. From February to August 2008 he was a Visiting Scholar at the University of Houston, TX, USA. From 2011 to 2014, he was a researcher at the Institute d'Electronique et de Télécommunications de Rennes (IETR), France. Since September 2014 he is at Sorbonne Université, Paris, France where he is a Professor.

His scientific interests involve antenna design and numerical methods for wave propagation and scattering in complex structures; namely, periodic Green's function computation, modal properties of multilayered structures, full-wave methods for SIW, modeling and design of periodic structures with higher symmetries.

Dr. Valerio is currently serving as an Associate Editor for the IEEE Transactions on Antennas and Propagation and the IEEE Access journals, and is the Main Chair of the COST Action SyMat on "Future communications with higher symmetric engineered artificial materials". In 2008 Dr. Valerio was the recipient of the "Leopold B. Felsen Award for Excellence in Electrodynamics." In 2009 he was a finalist for the "Young Engineering Prize" at the European Microwave Conference. In 2010 he was the recipient of the "Barzilai Prize" for the best paper at the National Italian Congress of Electromagnetism (XVIII RiNEM). In 2014, he was the recipient of the RMTG Award for junior researchers presented at the IEEE Antennas and Propagation Society Symposium, Memphis, TN. In 2018 and 2020, he was a co-author of the best papers in Electromagnetic and Antenna theory at the European Conference on Antennas and Propagation. In 2022, he was a co-author of the Best Student Paper Award at the 16th European Conference on Antennas and Propagation.